



1 **Ammonia emissions and depositions over the contiguous United States derived**  
2 **from IASI and CrIS using the directional derivative approach**

3 Zitong Li<sup>1,2</sup>, Kang Sun<sup>3,4\*</sup>, Kaiyu Guan<sup>1,2,5,6\*</sup>, Sheng Wang<sup>1,2</sup>, Bin Peng<sup>1,2,5,7</sup>, Lieven Clarisse<sup>8</sup>,  
4 Martin Van Damme<sup>8,9</sup>, Pierre-François Coheur<sup>9</sup>, Karen Cady-Pereira<sup>10</sup>, Mark W. Shephard<sup>11</sup>,  
5 Mark Zondlo<sup>12</sup>, Daniel Moore<sup>12</sup>

6 <sup>1</sup>Agroecosystem Sustainability Center, Institute for Sustainability, Energy, and Environment,  
7 University of Illinois Urbana-Champaign, Urbana, IL, USA.

8 <sup>2</sup>Department of Nature Resources and Environmental Sciences, College of Agricultural,  
9 Consumer and Environmental Sciences, University of Illinois Urbana-Champaign, Urbana, IL,  
10 USA.

11 <sup>3</sup>Department of Civil, Structural and Environmental Engineering, University at Buffalo, Buffalo,  
12 NY, USA.

13 <sup>4</sup>Research and Education in Energy, Environment and Water Institute, University at Buffalo,  
14 Buffalo, NY, USA.

15 <sup>5</sup>National Center for Supercomputing Applications, University of Illinois Urbana-Champaign,  
16 Urbana, IL, USA.

17 <sup>6</sup>Department of Computer Science, University of Illinois Urbana-Champaign, Urbana, IL, USA.

18 <sup>7</sup>Department of Crop Sciences, University of Illinois Urbana-Champaign, Urbana, IL, USA.

19 <sup>8</sup>Université libre de Bruxelles (ULB), BLU-ULB research Center, Spectroscopy, Quantum  
20 Chemistry and Atmospheric Remote Sensing (SQUARES), Brussels, Belgium

21 <sup>9</sup>Royal Belgian Institute for Space Aeronomy (BIRA-IASB), Brussels, Belgium.

22 <sup>10</sup>Atmospheric and Environmental Research, Lexington, MA, USA.

23 <sup>11</sup>Environment and Climate Change Canada, Toronto, ON, Canada.

24 <sup>12</sup>Department of Civil and Environmental Engineering, Princeton University, Princeton, NJ,  
25 USA.

26 Corresponding authors: Kang Sun (kangsun@buffalo.edu), Kaiyu Guan (kaiyug@illinois.edu)

27

28 **Abstract**

29 Atmosphere ammonia (NH<sub>3</sub>), primarily emitted from agriculture, poses  
30 significant threats to ecosystems, climate, and human health through nitrogen  
31 deposition and secondary aerosol formation. NH<sub>3</sub> flux estimates remain highly  
32 uncertain due to limited direct observations and complex emission–deposition  
33 processes. Here, we estimated NH<sub>3</sub> fluxes over the contiguous United States using  
34 satellite observations from the Infrared Atmospheric Sounding Interferometer (IASI,  
35 2008–2022) and Cross-track Infrared Sounder (CrIS, 2012–2022). By applying a  
36 directional derivative approach, we minimized the impact of offsets in satellite-derived  
37 vertical column densities. Our results highlight major agricultural emission hotspots,  
38 including the San Joaquin Valley in California, the Snake River Valley in Idaho, the  
39 Texas panhandle, the Great Plains, Southeastern Pennsylvania, and Eastern North



40 Carolina.  $\text{NH}_3$  removal was predominantly driven by deposition near source areas  
41 rather than chemical transformation, with strong sinks in vegetation-dense regions  
42 such as forests, grasslands, shrublands, and wetlands. Seasonal flux variations  
43 showed peaks in warm months and lower values in winter, driven by temperature-  
44 dependent volatilization from livestock production and fertilizer application. Satellite-  
45 based estimates aligned well with bottom-up inventories, effectively capturing spatial  
46 and seasonal patterns while revealing additional insights into key flux hotspots and  
47 peak seasons. CrIS consistently reported higher fluxes than IASI, especially in spring,  
48 reflecting differences in their overpass times. Combining IASI (morning overpass) and  
49 CrIS (midday overpass) observations enables a better understanding of diurnal  $\text{NH}_3$   
50 flux dynamics. These findings provide critical insights into  $\text{NH}_3$  spatiotemporal  
51 variabilities, complementing inventory-based approaches and informing nitrogen  
52 management and environmental policy, particularly in regions with limited ground-  
53 based monitoring.

#### 54 **1. Introduction**

55 Atmospheric  $\text{NH}_3$  is the most abundant alkaline gas (Asman et al., 1998; Sutton  
56 et al., 2020), and a major component of reactive nitrogen (Galloway et al., 2004). It is  
57 removed primarily through two pathways: deposition and chemical transformation.  
58 Deposition occurs when atmospheric  $\text{NH}_3$  is taken up by surfaces via dry or wet  
59 processes near its emission sources. Chemical removal involves reactions with sulfuric,  
60 nitric, and hydrochloric acids (Loubet et al., 2009), forming particulate ammonium  
61 ( $\text{NH}_4^+$ ) and secondary pollutants (Behera and Sharma, 2010; Wang et al., 2015).  
62 Global  $\text{NH}_3$  emissions have more than doubled since pre-industrial times (Galloway et  
63 al., 2003), driving a cascade of environmental consequences.  $\text{NH}_3$  deposition and its  
64 secondary chemical products contribute to ecosystem eutrophication and soil  
65 acidification, disrupting natural nutrient cycles and reducing biodiversity (van Breemen  
66 et al., 1982; Heil and Diemont, 1983; Sutton et al., 2008). These processes degrade  
67 air quality, threaten human health (Ma et al., 2021), and influence climate through  
68 radiative forcing alterations (Erisman et al., 2013; Gong et al., 2024).

69  $\text{NH}_3$  is emitted from various sources, including domestic animals (40%),  
70 synthetic fertilizers (17%), biomass burning (11%), natural sources (19%), crops (7%),  
71 and humans and pets (5%) (Bouwman et al., 1997). However, large-scale ground-  
72 based measurements of  $\text{NH}_3$  emissions are sparse due to the challenges associated  
73 with accurately capturing gaseous  $\text{NH}_3$ . Observations of  $\text{NH}_3$  fluxes are further  
74 constrained by its sharp spatial gradients and short tropospheric lifetime, typically of  
75 only a few hours (Adams et al., 2019; Wang et al., 2023). Regional and global  $\text{NH}_3$   
76 fluxes are often estimated using bottom-up approaches that rely on emission factors  
77 and spatial allocation of  $\text{NH}_3$ -emitting activities (Liu et al., 2022). However, these  
78 estimates have large uncertainties, reaching up to 50% (Bouwman et al., 1997). A  
79 major source of uncertainty is the lack of reliable statistics on fertilizer use and animal  
80 waste production. Regional variations in agricultural practices complicate scaling local  
81 observations to global estimates (Luo et al., 2022). Further challenges arise from a



82 limited understanding of emissions from natural sources and biomass burning  
83 (Dentener and Crutzen, 1994) and the dependence of  $\text{NH}_3$  volatilization on  
84 environmental conditions (Vira et al., 2022).

85 Advances in satellite-based atmospheric retrievals have introduced powerful  
86 tools for estimating trace gas fluxes, enabling large-scale investigation of gas  
87 dynamics. For example, the Infrared Atmospheric Sounding Interferometer (IASI) and  
88 the Cross-track Infrared Sounder (CrIS) have identified large  $\text{NH}_3$  point sources  
89 worldwide that were absent from bottom-up inventories (Van Damme et al., 2018;  
90 Dammers et al., 2019). Chemical transport models (CTMs) have been widely  
91 employed to derive gas fluxes from satellite observations (Cao et al., 2020, 2022; Chen  
92 et al., 2021; Marais et al., 2021). However, the computational demands of running  
93 CTMs at fine temporal and spatial scales pose significant limitations in fully leveraging  
94 the coverage and resolutions of new-generation satellite products. To complement  
95 CTMs, observational-data-driven approaches have been developed to derive gas  
96 emissions directly from satellite Level 2 products. The flux divergence method, for  
97 example, has been used to estimate  $\text{NO}_x$  fluxes (Beirle et al., 2019, 2021). Closely  
98 related to the flux divergence method, the directional derivative approach estimates  
99 fluxes with additional agility (Ayazpour et al., 2024; Sun, 2022) and demonstrates  
100 broad applicability across various atmospheric species and regions (Lonsdale and Sun,  
101 2023).

102 In this study, we applied the directional derivative approach to estimate  $\text{NH}_3$   
103 fluxes across the contiguous United States (CONUS). Using observations from two  
104 space-based instruments, IASI and CrIS, we derived top-down  $\text{NH}_3$  fluxes at fine  
105 spatial ( $0.1^\circ$  grid) and temporal (daily) resolutions. This study addresses the following  
106 questions: 1) How accurately can satellite observations from IASI and CrIS be used to  
107 estimate  $\text{NH}_3$  fluxes? 2) What are the spatiotemporal patterns of  $\text{NH}_3$  fluxes over the  
108 CONUS? Our findings aim to enhance the understanding of reactive nitrogen cycling  
109 and provide valuable information for environmental and policy applications.

## 110 **2. Data and Methods**

### 111 **2.1 Data**

112 IASI and CrIS datasets use distinct retrieval approaches, providing two  
113 independent datasets and complementary perspectives for analyzing  $\text{NH}_3$  flux patterns.  
114 IASI onboard the Metop-A/B/C meteorological payload was launched by the European  
115 Organisation for the Exploitation of Meteorological Satellites (EUMETSAT), starting in  
116 October 2006. Operating in a polar orbit, IASI provides global coverage with two  
117 overpass times daily, morning (09:30 local solar time, LST) and at night (21:30 LST).  
118 The instrument features a circular footprint on ground of 12 km along the satellite track  
119 and a swath width of 2200 km ( $\pm 48.3^\circ$ ) (Clerbaux et al., 2009). IASI measurements  
120 generate vertical column densities (VCDs) of  $\text{NH}_3$  using machine learning-based  
121 retrieval algorithms. We utilized daytime (09:30 LST)  $\text{NH}_3$  VCD measurements over  
122 the CONUS from January 2008 to December 2022. The data was sourced from the  
123 Level 2 reanalysis product of the ANNI- $\text{NH}_3$ -v4R dataset (Clarisse et al., 2023).



124 Additionally, we excluded Metop-A data after 2019 due to a drift in Metop-A's overpass  
125 time towards the end of its operational life. CrIS is onboard the Suomi-NPP, NOAA-20  
126 and NOAA-21 satellites, with the first instrument launched in October 2011. It also  
127 operates in a polar orbit with two overpass times daily, early afternoon (13:30 LST)  
128 and after midnight (01:30 LST). CrIS features a swath width identical to IASI (2200 km)  
129 and a similar ground pixel resolution (14 km circular pixels at nadir). NH<sub>3</sub> VCDs are  
130 generated using the fast physical retrieval (CFPR) approach (Shephard and Cady-  
131 Pereira, 2015; Shephard et al., 2020). We used daytime (13:30 LST) NH<sub>3</sub> VCDs  
132 measured by CrIS-NPP and CrIS-NOAA-20 over the CONUS for the period from June  
133 2012 to December 2022. The dataset was derived from the Level 2 CrIS NH<sub>3</sub> version  
134 1.6.4 product.

135 We used gridded monthly NH<sub>3</sub> emission inventories from the Harmonized  
136 Emissions Component (HEMCO) 3.0 for 2016 with a spatial resolution of 0.1° (Lin et  
137 al., 2021). HEMCO converts publicly available emissions data, such as SMOKE  
138 outputs, into inputs compatible with atmospheric models like GEOS-Chem. The  
139 inventory integrates data from the National Emissions Inventory (NEI) and includes  
140 key NH<sub>3</sub> sources such as agriculture, industry, and natural emissions. Comparing  
141 these bottom-up estimates with satellite-derived fluxes provides insights into their  
142 consistency and helps assess the utility of satellite-based estimates.

143 This study also incorporated additional datasets to support NH<sub>3</sub> flux estimation  
144 and analysis. Hourly horizontal wind data at 100 and 10 m above the surface was  
145 utilized to estimate NH<sub>3</sub> fluxes from VCD observations. The data was obtained from  
146 the ERA5 reanalysis at a spatial resolution of 0.25° (Hersbach et al., 2020) spanning  
147 2008 to 2022. The 2021 release of the National Land Cover Database (NLCD) with a  
148 resolution of 30 meters was used to analyze the spatial patterns of NH<sub>3</sub> fluxes across  
149 different land cover types. Land and water mask data from the North American Land  
150 Data Assimilation System (NLDAS) unified mask were used to exclude water body  
151 data due to the larger noise of the satellite retrievals over these areas.

## 152 **2.2 NH<sub>3</sub> flux estimations**

### 153 **2.2.1 Directional derivative approach**

154 The derivation of emissions ( $E$ ) from satellite-observed column amounts ( $\Omega$ ) is  
155 grounded in the principle of mass conservation as in Eq. (1). This approach considers  
156 the physical and chemical processes affecting gas distribution, incorporating horizontal  
157 transport, topography, and chemical transformation. The first term ( $DD$ ) captures the  
158 role of wind in transporting NH<sub>3</sub> horizontally, representing the directional derivatives of  
159 the column amounts ( $\Omega$ ) with respect to horizontal wind vectors ( $\vec{u}$ , 100 m winds  
160 sampled from ERA5) within the planetary boundary layer. The second term accounts  
161 for the directional derivatives of the surface altitudes ( $z_0$ , obtained from Level 2 satellite  
162 data) relative to near-surface wind vectors ( $\vec{u}_0$ , 10 m winds sampled from ERA5), which  
163 is denoted as  $DD_{topo}$  combined with  $DD$ . This component captures the influence of  
164 terrain on NH<sub>3</sub> movement. For example, variations in elevation can create localized  
165 gradients that resemble NH<sub>3</sub> fluxes. The third term reflects chemical interactions



166 between  $\text{NH}_3$  and atmospheric acids, resulting in the formation of particulate matter,  
 167 and is referred to as  $DD\_chem$  along with the other terms. The full derivation of Eq. (1)  
 168 is detailed in Sun (2022) and further explained by Ayazpour et al. (2024).

169

$$\langle E \rangle = \underbrace{\langle \vec{u} \cdot (\nabla \Omega) \rangle}_{DD} + \underbrace{X \langle \Omega \vec{u}_0 \cdot (\nabla z_0) \rangle + k \langle \Omega \rangle}_{DD\_chem} \quad (1)$$

170

171

172 Here  $X$  and  $k$  represent the inverse scale height and inverse chemical lifetime,  
 173 in which scale height represents the characteristic height of the species' vertical  
 174 distribution, and chemical lifetime represents the average time before the species  
 175 being removed by chemical reactions.  $\langle \rangle$  denotes the spatiotemporal averaging  
 176 operator already implemented in the physical oversampling framework (Sun et al.,  
 177 2018). This method leverages the spatial variability of individual orbits and the data  
 178 record to reduce noise and smooth spatial gradients in the gridded product. We  
 179 employed the oversampling approach to aggregate Level 2 satellite data into a gridded  
 180 Level 3 product at a  $0.1^\circ$  resolution on a daily scale. Data from IASI and CrIS were  
 181 treated separately, but when multiple IASI and CrIS instruments were available on the  
 182 same day, their data were merged together. Each Level 2 pixel was inflated spatially  
 183 by a factor of 2 along both the major and minor axes of the ellipses, effectively filling  
 184 observational gaps and reducing noise. By smoothing spatial gradients, this method  
 185 enables the generation of a more continuous and representative Level 3  $\text{NH}_3$  product.

186 To estimate gas flux, the inverse scale height ( $X$ ) and inverse chemical lifetime  
 187 ( $k$ ) were determined using a linear regression approach. At locations where the  
 188 emission term ( $E$ ) was negligible compared to other terms ( $< 1 \times 10^{-9} \text{ mol m}^{-2}$ , Fig.  
 189 S1), Eq. (1) can be reformulated into a multilinear regression model by omitting the  
 190 emission term:

191

$$\langle \vec{u} \cdot (\nabla \Omega) \rangle = \beta_0 + \beta_1 \langle \Omega \vec{u}_0 \cdot (\nabla z_0) \rangle + \beta_2 \langle \Omega \rangle + \varepsilon \quad (2)$$

192

193 Here  $\beta_1$  corresponds to the negative inverse scale height ( $-X$ ), and  $\beta_2$   
 194 represents the negative inverse chemical lifetime ( $-k$ ). The  $\beta_0$  and  $\varepsilon$  account for the  
 offset and random error, respectively, in the  $DD$  term  $\langle \vec{u} \cdot (\nabla \Omega) \rangle$ .

195 We conducted a two-step fitting process to estimate  $\text{NH}_3$  fluxes over the  
 196 CONUS (Lonsdale and Sun, 2023). The first fitting step focused on  $\beta_1$  since the fitting  
 197 results for  $\beta_2$  are usually noisy. This fitting was limited to rough terrains with  
 198  $0.001 \text{ m s}^{-1} < \langle \vec{u}_0 \cdot (\nabla z_0) \rangle < 0.1 \text{ m s}^{-1}$ . Once  $\beta_1$  was determined and then fixed, and  
 199 the second step focused on  $\beta_2$ . This step was conducted in flat terrains with moderate  
 200  $\text{NH}_3$  column amounts and minimal  $\text{NH}_3$  emissions to isolate chemical transformation.  
 201 To address the challenges associated with a low signal-to-noise ratio, the fitting was  
 202 performed over extended time intervals. Daily flux components, including  $\langle \vec{u} \cdot (\nabla \Omega) \rangle$ ,  
 203  $\langle \Omega \vec{u}_0 \cdot (\nabla z_0) \rangle$  and  $\langle \Omega \rangle$ , were first calculated at a spatial resolution of  $0.1^\circ$ . These values  
 204 were then aggregated into six-month intervals for IASI and four-month intervals for  
 205 CrIS, striking a balance between temporal resolution and noise reduction.



## 206 2.2.2 Uncertainty analysis

207 To estimate the uncertainty in  $DD$ , we calculated directional derivatives in both  
208 the zonal/meridional directions ( $\vec{x}/\vec{y}$ ) and the diagonal directions ( $\vec{r}/\vec{s}$ ). The final  $DD$   
209 value was determined as the mean of the directional derivatives calculated along the  
210  $\vec{x}/\vec{y}$  and  $\vec{r}/\vec{s}$  directions:

$$211 \quad DD = \text{mean}(DD_{\vec{x}/\vec{y}}, DD_{\vec{r}/\vec{s}}) \quad (3)$$

$$212 \quad DD_{\vec{x}/\vec{y}} = \vec{u} \cdot (\nabla\Omega)_{\vec{x}/\vec{y}} = u_x \frac{\partial\Omega}{\partial x} + u_y \frac{\partial\Omega}{\partial y} \quad (4)$$

$$213 \quad DD_{\vec{r}/\vec{s}} = \vec{u} \cdot (\nabla\Omega)_{\vec{r}/\vec{s}} = u_r \frac{\partial\Omega}{\partial r} + u_s \frac{\partial\Omega}{\partial s} \quad (5)$$

214 The difference between  $DD_{\vec{x}/\vec{y}}$  and  $DD_{\vec{r}/\vec{s}}$  was used to estimate the random  
215 errors ( $\sigma$ ) of  $DD$ :

$$216 \quad \sigma = [\text{std}(DD_{\vec{x}/\vec{y}} - DD_{\vec{r}/\vec{s}})]/2 \quad (6)$$

217 We evaluated  $\text{NH}_3$  fluxes at multiple spatial resolutions, including  $0.2^\circ$ ,  $0.1^\circ$ , and  
218  $0.04^\circ$ . Consistent spatiotemporal patterns were observed across all grid scales (Fig.  
219 S2). A resolution of  $0.1^\circ$  was selected as the optimal balance, ensuring sufficient data  
220 coverage while effectively capturing spatial gradients in  $\text{NH}_3$  fluxes (Wang et al., 2023).

## 221 2.3 Spatiotemporal pattern analysis

222 To analyze the spatial patterns of  $\text{NH}_3$  fluxes, we focused on the period from  
223 September 2019 to April 2021. This timeframe was selected because both IASI and  
224 CrIS observations of  $\text{NH}_3$  VCDs provided the most extensive data coverage, enabling  
225 a more reliable comparison between the two datasets. We also compared the spatial  
226 patterns of satellite-based  $\text{NH}_3$  fluxes with bottom-up inventory  $\text{NH}_3$  emissions and  
227 land cover types. This comparison allows us to evaluate the consistency of satellite-  
228 derived flux estimates with known  $\text{NH}_3$  sources and their relationship to land use and  
229 vegetation cover.

230 For the temporal pattern analysis, we utilized the full observational periods of  
231 the datasets: January 2008 to December 2022 for IASI and June 2012 to December  
232 2022 for CrIS. This extended temporal coverage allows for a comprehensive  
233 understanding of  $\text{NH}_3$  flux trends over time. To analyze the temporal patterns of  $\text{NH}_3$   
234 emission/deposition rates across high-flux regions, we calculated regional  
235 emission/deposition rates by spatially integrating the fluxes within the source/sink  
236 areas of each region. We examined the seasonal patterns of  $\text{NH}_3$  emission/deposition  
237 rates in both source and sink areas. These areas were defined based on the  
238 uncertainty in  $DD$  quantified in Eq. 6. We classified locations where both IASI- and  
239 CrIS-derived  $\text{NH}_3$  fluxes exceeded  $2\sigma$  as source regions and locations with both fluxes  
240 lower than  $-2\sigma$  as sink regions. Additionally, we investigated the seasonal variations  
241 in  $\text{NH}_3$  emission/deposition rates derived from IASI and CrIS observations. These were  
242 compared with seasonal signals in inventory data to evaluate the consistency between  
243 top-down and bottom-up approaches.



## 244 3. Results

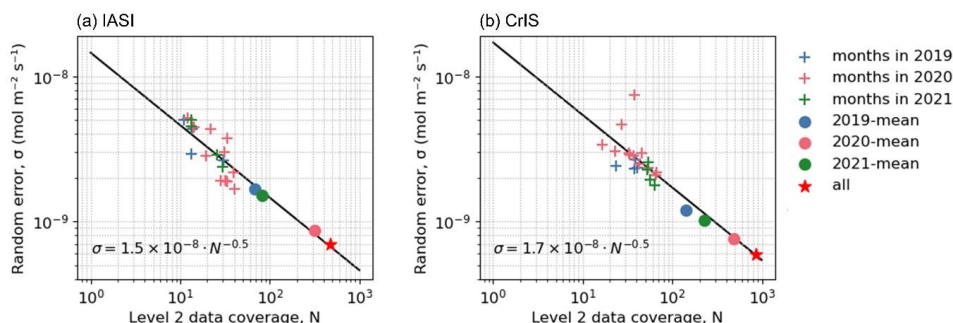
### 245 3.1 NH<sub>3</sub> flux estimation

246 In this study, we used the  $DD_{topo}$  term as our estimate for NH<sub>3</sub> fluxes, and the  
247 chemical loss term ( $k\langle\Omega\rangle$ ) was excluded due to its negligible contribution and poor  
248 fitting performance. Specifically, the derived  $k$  values and its fitting  $R^2$  were  
249 consistently near zero, indicating minimal contribution of chemical loss for the overall  
250 fluxes (Fig. S3). In contrast, the wind-topography term ( $\langle\Omega\vec{u}_0 \cdot (\nabla z_0)\rangle$ ) proved essential  
251 for addressing topographic biases in mountainous regions (Fig. S4). Estimated NH<sub>3</sub>  
252 scale heights generally ranged from 1 to 2 km (Fig. S5), approximating the planetary  
253 boundary layer height. Higher scale heights were observed when only one IASI  
254 instrument was operational as well as during winter months in CrIS data, possibly due  
255 to weak thermal contrast.

256 Fig. 1 shows the random errors, estimated through Eq. 6, in IASI- (a) and CrIS-  
257 based (b) fluxes over the CONUS from 2019 to 2021. These random errors were  
258 calculated separately over monthly, annual, and total aggregated flux fields and plotted  
259 against the mean coverage of Level 2 pixels used in the aggregation. These mean  
260 coverage values were denoted by  $N$  and roughly correspond to the number of satellite  
261 overpasses. Both IASI and CrIS observations demonstrated improved precision (lower  
262 random errors) with increasing data coverage. The black lines in Fig. 1 represent the  
263 theoretical scaling relationship,  $\sigma = \sigma_0 / \sqrt{N}$ , where  $\sigma_0$  is the scaling factor derived  
264 from the random errors of the monthly values:

$$265 \quad \sigma_0 = \exp(\text{mean}(\log(\sigma_i)) + 0.5 \cdot \text{mean}(\log(N_i))) \quad (7)$$

266 where  $\sigma_i$  and  $N_i$  represent the random errors and mean Level 2 data coverage for  
267 month  $i$ . If the random errors across different aggregation levels align with the  $1/\sqrt{N}$   
268 scaling, it suggests that the random errors are independent and random. This  
269 alignment in Fig. 1 highlights the importance of extensive spatial and temporal  
270 coverage for reliable flux estimation. Additionally, the intercept of the black line with  
271 the vertical line at  $N = 1$  provides the theoretical precision ( $\sigma_0$ ) of flux estimated by a  
272 single, gap-free overpass of the satellite instrument. IASI showed slightly better single-  
273 overpass precision at  $1.5 \times 10^{-8}$  mol m<sup>2</sup> s<sup>-1</sup> for IASI, compared with  $1.7 \times 10^{-8}$  mol m<sup>2</sup> s<sup>-1</sup>  
274 for CrIS. However, the random errors are generally lower for CrIS when aggregated  
275 to the same intervals due to its denser Level 2 coverage than IASI.

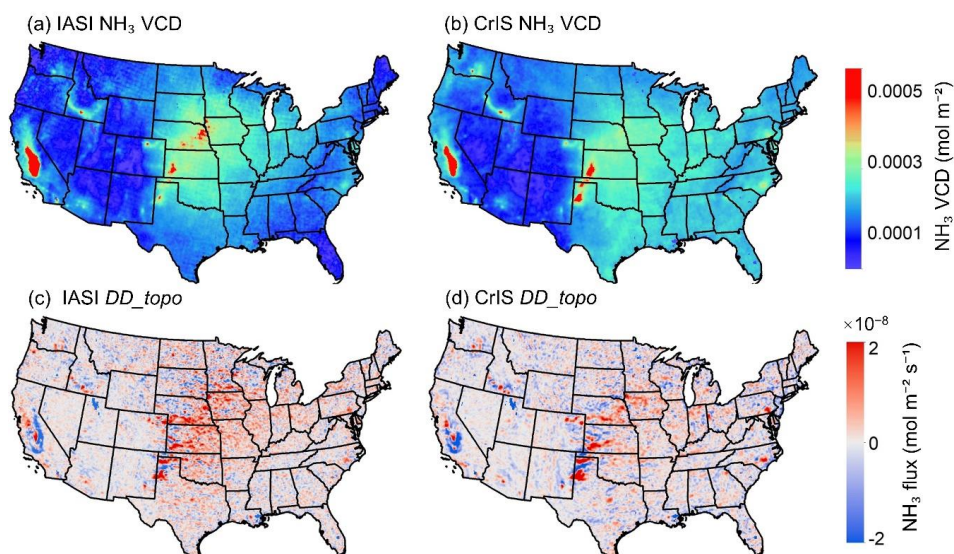


276

277 Figure 1. The relationship between random error ( $\sigma$ ) and data coverage ( $N$ ) for IASI  
 278 (a) and CrIS (b) records. Dots represent random errors at various aggregation levels  
 279 (monthly, annual, and total). The black lines represent the theoretical scaling  
 280 relationship,  $\sigma = \sigma_0 / \sqrt{N}$ , where  $\sigma_0$  denotes the single-overpass precision.

### 281 3.2 Spatiotemporal pattern of NH<sub>3</sub> flux over the CONUS

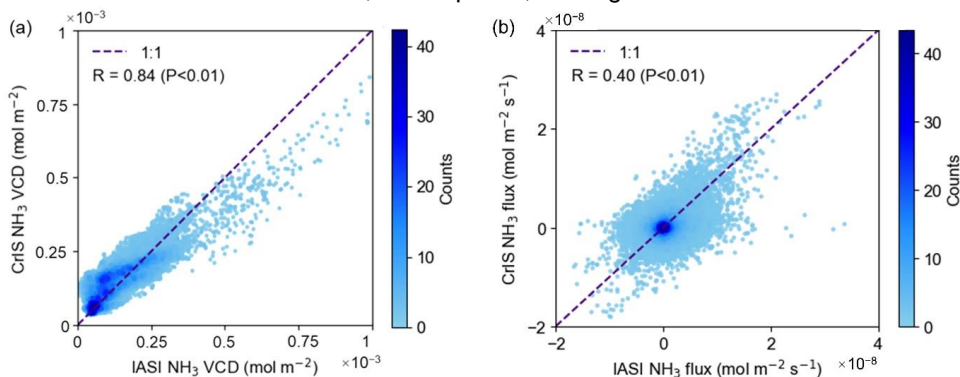
282 IASI and CrIS observations exhibited consistent hotspot regions in NH<sub>3</sub> VCDs  
 283 and fluxes (Fig. 2). Spatially continuous hotspots included the San Joaquin Valley in  
 284 California, the Snake River Valley in Idaho, the Texas panhandle and the Great Plains  
 285 (Fig. 4-7), all regions known for intensive livestock production and high nitrogen  
 286 fertilizer use (Liu et al., 2019). Discrete NH<sub>3</sub> emission hotspots also occurred in the  
 287 eastern United States, notably in Southeastern Pennsylvania and Eastern North  
 288 Carolina (Fig. 8, 9), where concentrated animal feeding operations (CAFOs) are  
 289 prevalent. Major NH<sub>3</sub> sinks were located near sources, highlighting the localized  
 290 deposition of NH<sub>3</sub> emissions. The primary sources of NH<sub>3</sub> emissions from satellite  
 291 observations showed strong consistency with those from bottom-up inventories (Fig.  
 292 S1), enhancing confidence in the reliability of satellite-based flux estimates for  
 293 identifying key emission regions.



294

295 Figure 2. IASI- (a, c) and CrIS- (b, d) derived  $\text{NH}_3$  VCD (a, b) and  $DD_{topo}$  flux (c, d)  
 296 averaged from Sep 2019 to Apr 2021 over the CONUS on a  $0.1^\circ$  grid.

297 Both  $\text{NH}_3$  VCDs and flux estimates showed significant spatial agreement in IASI  
 298 and CrIS, with correlation coefficients of  $R = 0.84$  for VCDs and  $R = 0.40$  for  $\text{NH}_3$  fluxes  
 299 ( $P < 0.01$ ; Fig. 3). Frequently there was an offset between VCDs from CrIS and IASI,  
 300 manifested as consistent shifts or proportional scaling differences (Fig. 3a), impacting  
 301 flux estimates in different ways. By concentrating on spatial gradients of VCDs, the  
 302 directional derivative approach minimizes the impact of these offsets and results in  
 303 comparable  $\text{NH}_3$  flux patterns across both datasets. The lower correlation for fluxes  
 304 compared to VCDs likely reflects additional noise introduced during flux estimation,  
 305 which relies on external datasets, assumptions, and signal differentiation.



306

307 Figure 3. Comparison of IASI- and CrIS-derived  $\text{NH}_3$  VCD (a) and flux (b) averaged  
 308 from Sep 2019 to Apr 2021.

309 The  $\text{NH}_3$  fluxes over the CONUS exhibited a clear seasonal pattern, with higher  
 310 fluxes observed in spring and summer and lower values during winter (Fig. S6). CrIS-

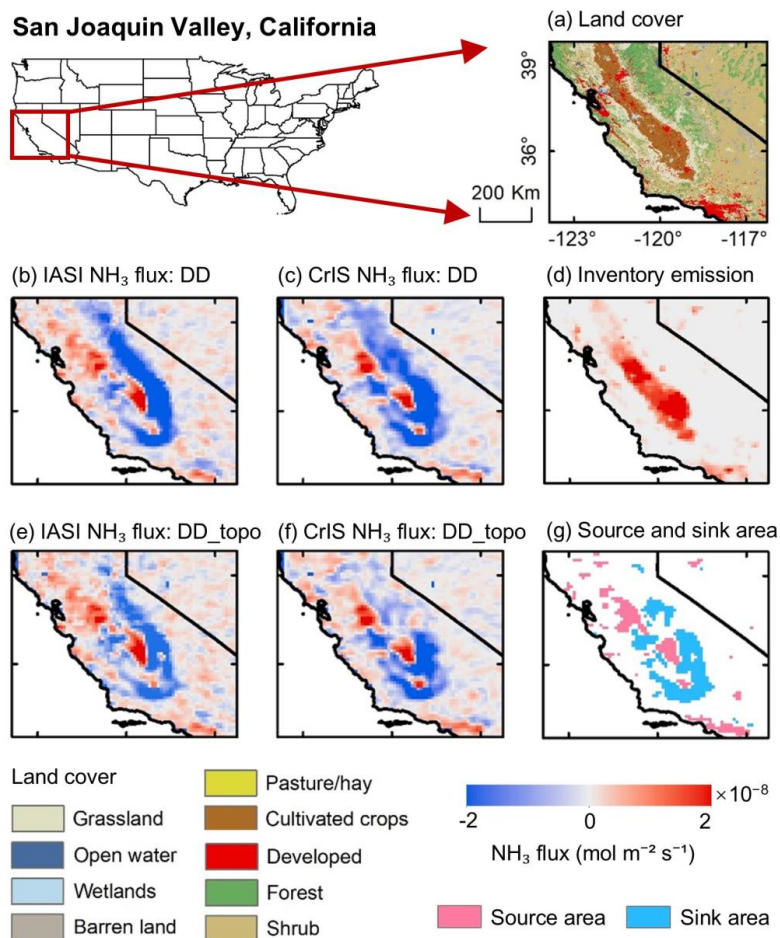


311 derived  $\text{NH}_3$  flux showed strong signals throughout spring and summer, reflecting  
312 consistent emissions during these warmer months. IASI-derived  $\text{NH}_3$  flux displayed a  
313 more pronounced peak during summer. This difference may be attributed to the  
314 instruments' distinct observational characteristics, such as overpass time, and  
315 sensitivities under varying seasonal conditions. These spatiotemporal patterns are  
316 studied more closely in high-flux regions in the following section.

### 317 **3.3 Spatiotemporal pattern of $\text{NH}_3$ flux in high-flux regions**

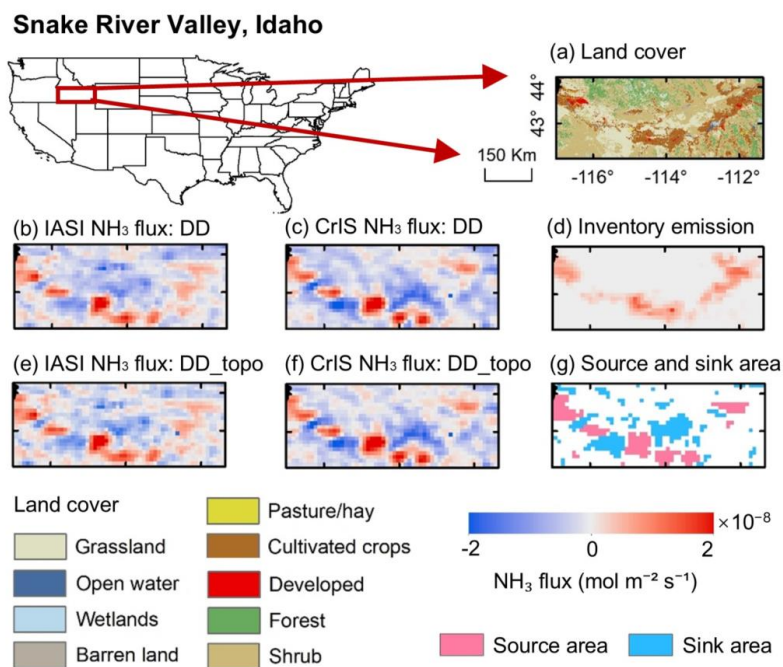
318 Both IASI and CrIS revealed consistent spatial patterns of  $\text{NH}_3$  sources and  
319 sinks across key high-flux regions (Fig. 4-9), closely linked to underlying land cover  
320 types. Agricultural lands emerged as dominant  $\text{NH}_3$  sources, while vegetated  
321 landscapes, including forests, shrublands, grasslands (Fig. 4-8), and wetlands (Fig. 9),  
322 predominantly served as  $\text{NH}_3$  sinks. These natural and managed ecosystems can  
323 capture  $\text{NH}_3$  through deposition processes near emission sources.

324 In areas with complex terrain, such as the mountainous regions near  
325 California's San Joaquin Valley, topographical artifacts were reduced when using  
326 *DD\_topo* instead of *DD* (Figure 4 b, c, e, f), while *DD\_topo* and *DD* exhibited similar  
327 flux values in flatter regions (Figure 5-9 b, c, e, f). Moreover, spatial patterns observed  
328 by IASI and CrIS closely align with bottom-up emission inventories, with correlation  
329 coefficients ranging from 0.38 to 0.78 over the key high-flux regions (Fig. S7),  
330 supporting the utility of satellite-derived flux estimates in characterizing  $\text{NH}_3$  flux  
331 dynamics.



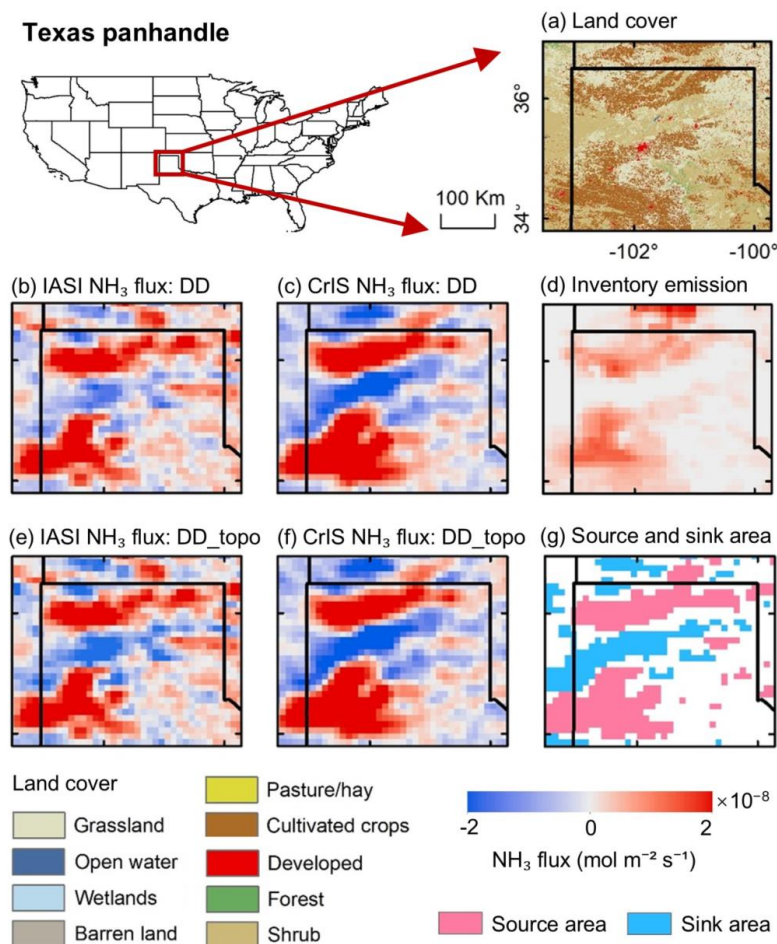
332

333 Figure 4. (a) Land cover types in the San Joaquin Valley in California. (b, c) *DD* and  
 334 (e, f) *DD\_topo* flux derived from IASI and CrIS  $\text{NH}_3$  records. (d)  $\text{NH}_3$  emission from  
 335 bottom-up inventory. (g) Source and sink areas of  $\text{NH}_3$  flux, defined as the outside  
 336 region of  $\pm 2\sigma$  of *DD* from IASI and CrIS.



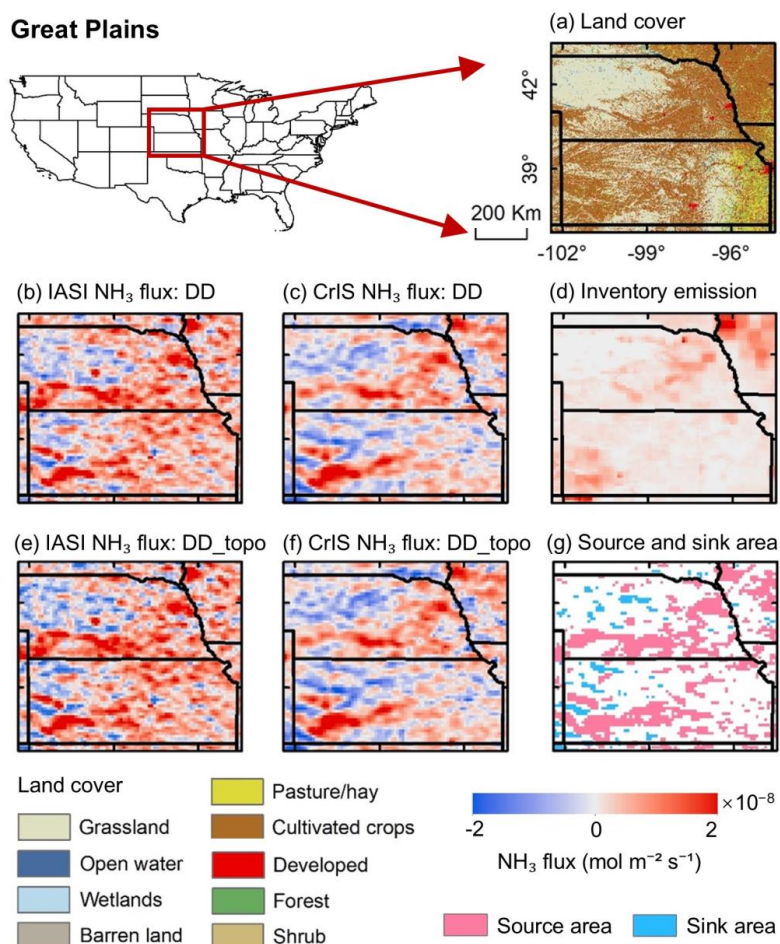
337

338 Figure 5. (a) Land cover types in the Snake River Valley in Idaho. (b, c) *DD* and  
 339 (e, f) *DD\_topo* flux derived from IASI and CrIS NH<sub>3</sub> records. (d) NH<sub>3</sub> emission from  
 340 bottom-up inventory. (g) Source and sink areas of NH<sub>3</sub> flux, defined as the outside  
 341 region of  $\pm 2\sigma$  of *DD* from IASI and CrIS.



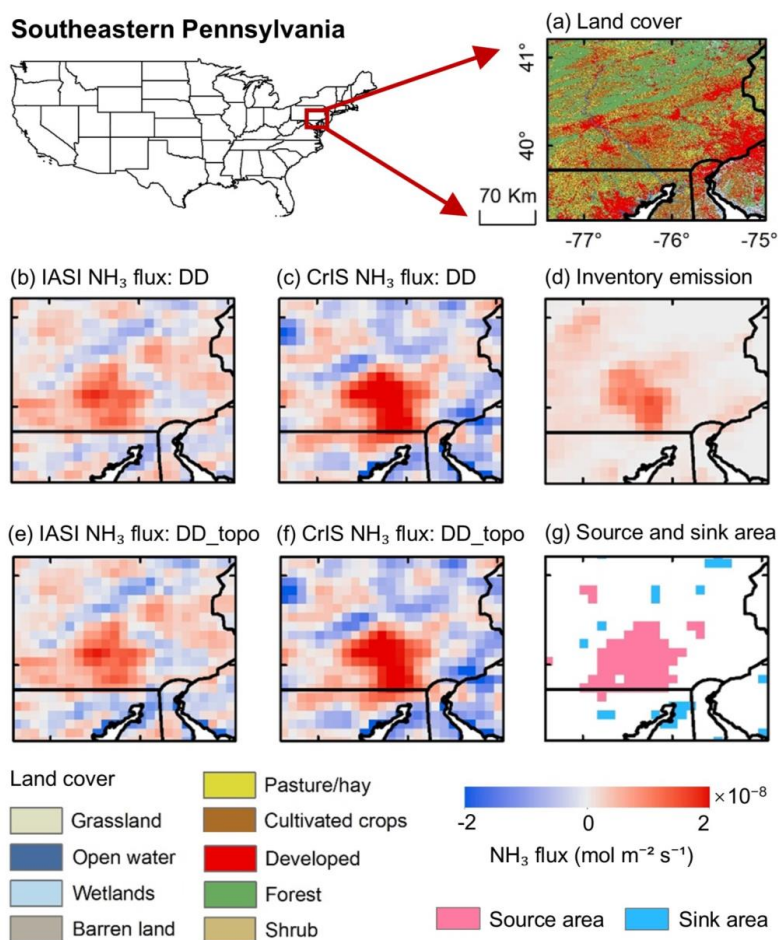
342

343 Figure 6. (a) Land cover types in the Texas panhandle. (b, c) *DD* and (e, f)  
 344 *DD\_topo* flux derived from IASI and CrIS  $\text{NH}_3$  records. (d)  $\text{NH}_3$  emission from bottom-  
 345 up inventory. (g) Source and sink areas of  $\text{NH}_3$  flux, defined as the outside region of  
 346  $\pm 2\sigma$  of *DD* from IASI and CrIS.



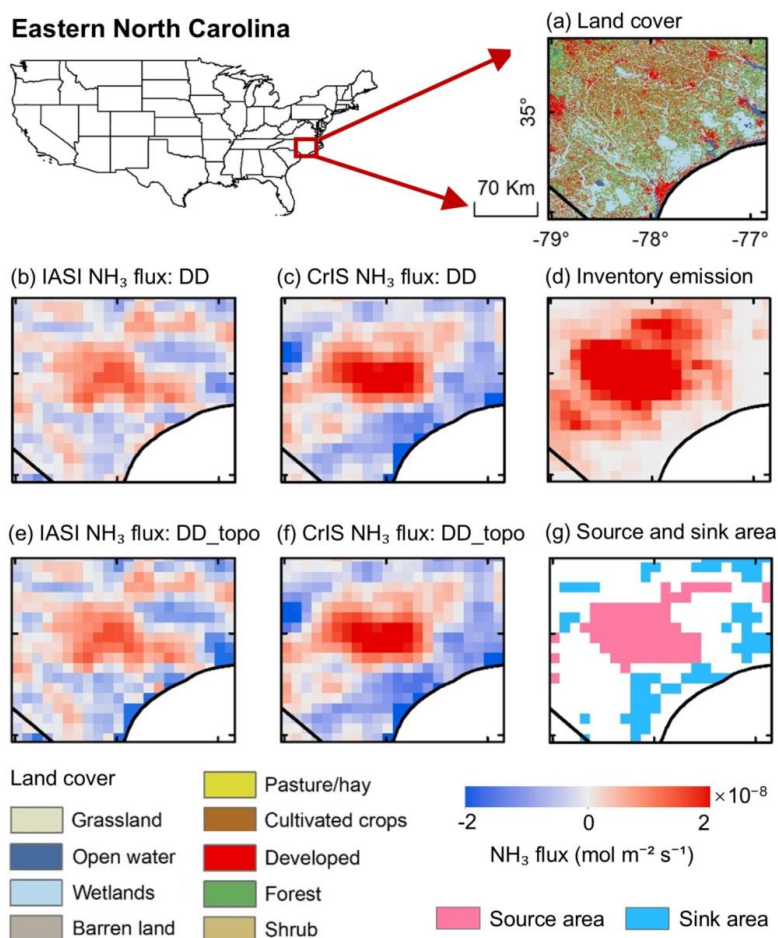
347

348 Figure 7. (a) Land cover types in the Great Plains. (b, c) *DD* and (e, f) *DD\_topo*  
 349 flux derived from IASI and CrIS NH<sub>3</sub> records. (d) NH<sub>3</sub> emission from bottom-up  
 350 inventory. (g) Source and sink areas of NH<sub>3</sub> flux, defined as the outside region of  $\pm 2\sigma$   
 351 of *DD* from IASI and CrIS.



352

353 Figure 8. (a) Land cover types in Southeastern Pennsylvania. (b, c) *DD* and (e, f)  
 354 *DD\_topo* flux derived from IASI and CrIS NH<sub>3</sub> records. (d) NH<sub>3</sub> emission from bottom-  
 355 up inventory. (g) Source and sink areas of NH<sub>3</sub> flux, defined as the outside region of  
 356 ±2σ of *DD* from IASI and CrIS.



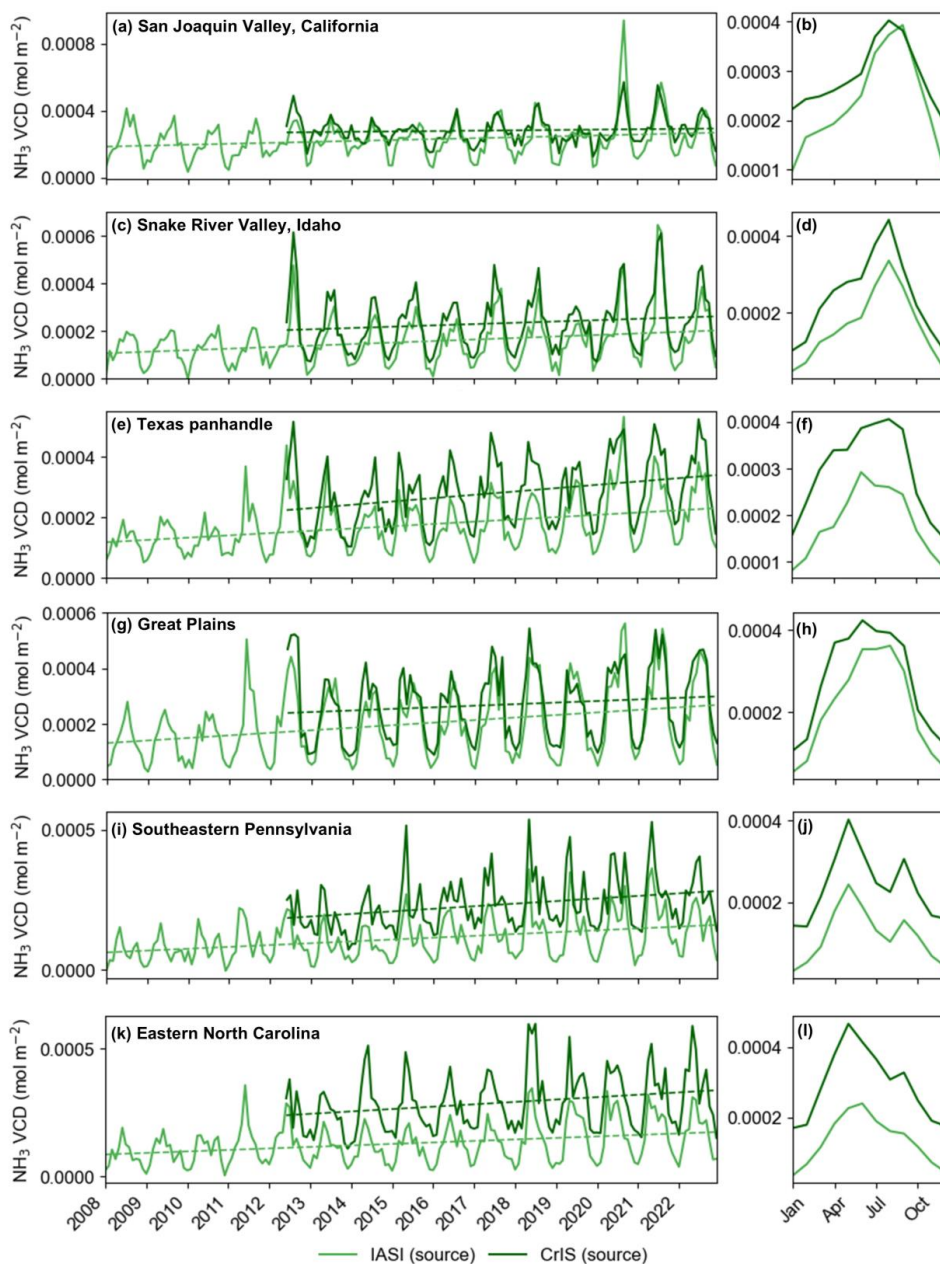
357

358 Figure 9. (a) Land cover types in Eastern North Carolina. (b, c) *DD* and (e, f)  
 359 *DD\_topo* flux derived from IASI and CrIS NH<sub>3</sub> records. (d) NH<sub>3</sub> emission from bottom-  
 360 up inventory. (g) Source and sink areas of NH<sub>3</sub> flux, defined as the outside region of  
 361 ±2σ of *DD* from IASI and CrIS.

362 Fig. 10 and 11 illustrate the temporal and seasonal patterns of NH<sub>3</sub> VCDs and  
 363 emission/deposition rates across major high-flux regions in the CONUS. Over time,  
 364 these regions exhibited upward trends in VCDs (Fig. 10), potentially indicating  
 365 increasing NH<sub>3</sub> emissions. Seasonal cycles in NH<sub>3</sub> VCDs were distinct across all  
 366 regions, with higher values in the warm seasons and lower values in winter, driven by  
 367 increased agricultural activities, such as livestock operations and fertilizer application,  
 368 and enhanced volatilization during higher temperatures. Observations from CrIS (dark  
 369 lines) and IASI (light lines) were generally aligned, though CrIS often reported higher  
 370 VCDs. Differences between CrIS and IASI were largely consistent across seasons, but  
 371 tended to be more pronounced in the warm months in regions such as the Texas  
 372 Panhandle and Great Plains (Fig. 10 f, h).

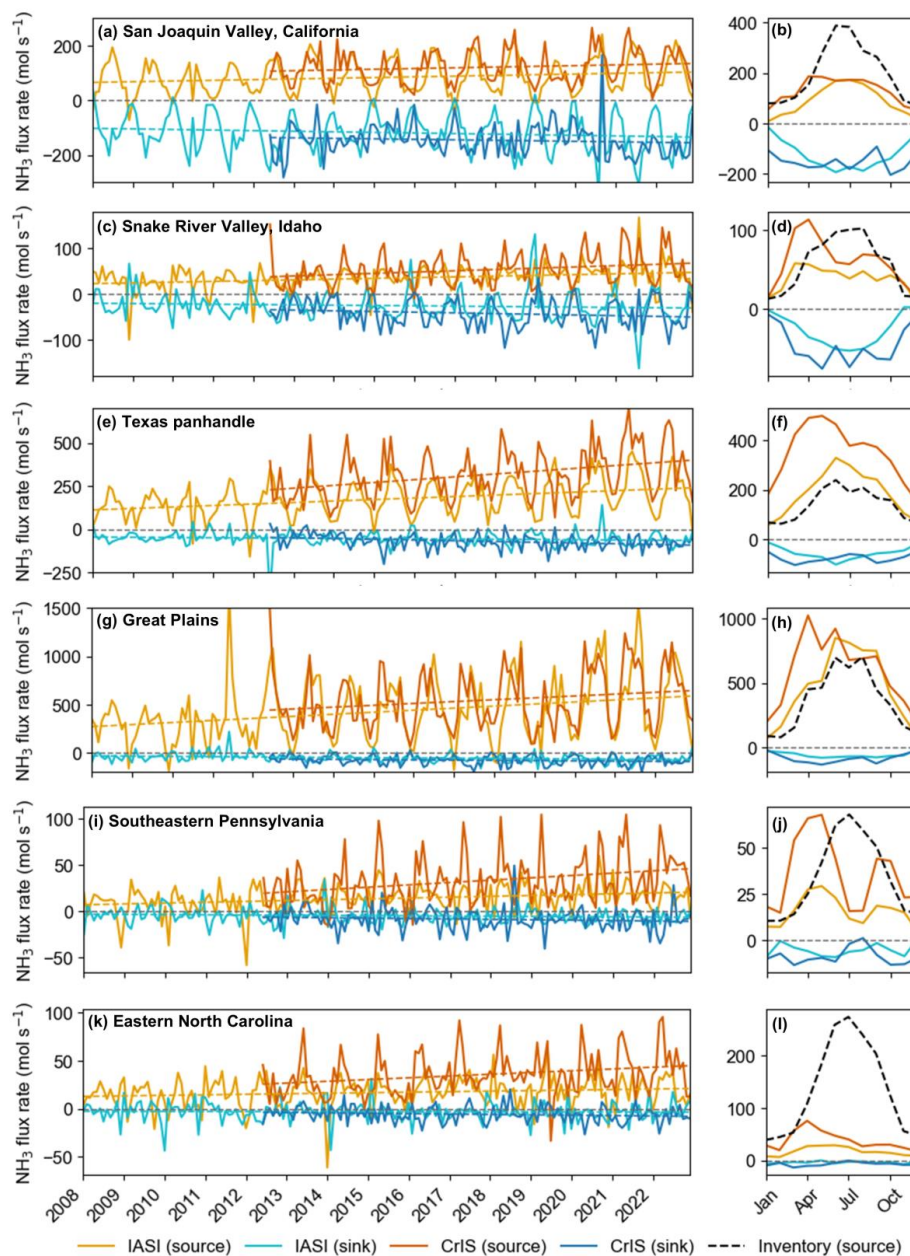


373            Satellite-derived  $\text{NH}_3$  fluxes, including emissions (positive fluxes, yellow lines)  
374 and depositions (negative fluxes, blue lines), exhibited increasing trends over time (Fig.  
375 11). Seasonal patterns in  $\text{NH}_3$  fluxes revealed mirrored those of VCDs, with emissions  
376 peaking in warm months due to heightened agricultural activity and elevated  
377 temperatures, while deposition rates also increased during this period, though with  
378 smaller magnitudes. This synchronization between emissions and deposition rates  
379 suggests that a significant proportion of emitted  $\text{NH}_3$  was deposited locally. A  
380 comparison with bottom-up inventory data revealed key differences. Satellite-based  
381 estimates captured diurnal patterns, with IASI observing morning emissions (09:30  
382 LST) and CrIS capturing midday emissions (13:30 LST), whereas inventory data  
383 represented modeled averages. In regions like the Texas Panhandle and Great Plains  
384 (Fig. 11 f, h), satellite observations showed higher seasonal emission peaks than  
385 inventory models, indicating potential underestimation of seasonal emissions in the  
386 inventories. Conversely, inventories overestimated emissions compared to satellite  
387 observations in the San Joaquin Valley and Eastern North Carolina (Fig. 11 b, l).  
388 Seasonality in inventory emissions was consistent with IASI observations in some  
389 regions, such as the Texas Panhandle and Great Plains (Fig. 11 f, h). However, in the  
390 Snake River Valley, Southeastern Pennsylvania, and Eastern North Carolina (Fig. 11  
391 d, j, l), inventory displayed entirely different seasonal signals compared to satellite data,  
392 underscoring the value of satellite observations in capturing the temporal dynamics of  
393 agricultural emissions. CrIS consistently observed larger  $\text{NH}_3$  emissions than IASI,  
394 while deposition differences were smaller. Notably, the difference between CrIS and  
395 IASI was most obvious in spring across all the regions. CrIS detected early spring  
396 peaks in regions like the Texas Panhandle and Great Plains (Fig. 11 f, h), which were  
397 not captured by IASI, highlighting variations in sensitivity between the two instruments.



398

399 Figure 10. Temporal series (a, c, e, g, i, k) and seasonal pattern (b, d, f, h, j, l) of NH<sub>3</sub>  
 400 VCD at source areas from IASI (light lines) and CrIS (dark lines) records in the San  
 401 Joaquin Valley in California (a, b), Snake River Valley in Idaho (c, d), Texas panhandle  
 402 (e, f), Great Plains (g, h), Southeastern Pennsylvania (i, j), and Eastern North Carolina  
 403 (k, l). The dashed lines represent trends derived using linear regression applied to the  
 404 monthly temporal series data.



405

406 Figure 11. Temporal series (a, c, e, g, i, k) and seasonal pattern (b, d, f, h, j, l) of NH<sub>3</sub>  
 407 emission/deposition rate from IASI (light lines) and CrIS (dark lines) records, and NH<sub>3</sub>  
 408 emission rate at source areas from bottom-up inventory (black dashed lines) in the  
 409 San Joaquin Valley in California (a, b), Snake River Valley in Idaho (c, d), Texas  
 410 panhandle (e, f), Great Plains (g, h), Southeastern Pennsylvania (i, j), and Eastern  
 411 North Carolina (k, l).



412 **4. Discussion**

413 **4.1 Robustness of satellite-based NH<sub>3</sub> flux estimates**

414 Our findings underscore the value of satellite observations in advancing the  
415 characterization of NH<sub>3</sub> fluxes. With the ability to produce flux estimates at relatively  
416 fine spatial and temporal scales, satellite datasets can help understand emission and  
417 deposition dynamics, thereby providing additional insights into seasonal variability that  
418 traditional bottom-up inventories often miss.

419 A key advancement of this work is the combined use of IASI (morning overpass)  
420 and CrIS (midday overpass). By combining these two instruments, it is possible to  
421 achieve quasi-diurnal coverage and capture the sub-daily variability of NH<sub>3</sub> fluxes that  
422 is challenging to discern with a single satellite product. This synergy is especially  
423 evident in spring, when the transition from cooler morning to warmer midday conditions  
424 can amplify NH<sub>3</sub> emissions. CrIS frequently shows an early-spring emission pulse that  
425 is less pronounced in IASI data, especially in areas with substantial emissions (Fig.  
426 11). Spring emerged as a critical transitional period, characterized by moderate  
427 temperature differences between IASI and CrIS observations (Fig. S8) and relatively  
428 high NH<sub>3</sub> fluxes (Fig. 10). A further strength of combining different instruments lies in  
429 the expanded data coverage. Our error analysis indicates a strong  $1/\sqrt{N}$  dependence  
430 of random errors (Fig. 1), suggesting that the flux uncertainties drop significantly with  
431 denser observations (Wang et al., 2023). By merging multiple overpasses and  
432 employing spatial smoothing through physical oversampling, we can substantially  
433 reduce random errors and enhance flux precision.

434 Our satellite-based approach demonstrates some advantages over bottom-up  
435 inventories, in which satellite-based observations detect finer-scale fluxes and uncover  
436 seasonal patterns not always well represented in inventory data. Previous studies have  
437 shown that top-down approaches using satellite observations significantly reduce  
438 uncertainties in emission estimates (Byrne et al., 2024; Evangeliou et al., 2021). Each  
439 method has unique strengths, and integrating them offers a robust pathway to make  
440 more reliable and comprehensive estimates (Tian et al., 2020). While bottom-up  
441 methods provide critical context on local processes such as fertilizer application  
442 (Zhang et al., 2018), satellite data can validate or refine emission factors and aid in  
443 reconciling regional to continental-scale uncertainties (Chen et al., 2021; Zhu et al.,  
444 2013).

445 Despite their advantages, infrared-based NH<sub>3</sub> satellite retrievals have certain  
446 limitations. For instance, weak thermal contrast and cooler thermal signals, common  
447 in winter, reduces the detection efficiency of the infrared sensors (Clarisse et al., 2010;  
448 Sutton et al., 2013). Overcoming these challenges requires ongoing refinements to  
449 retrieval algorithms, particularly in cloud screening and thermal contrast corrections.  
450 As satellite missions and retrieval techniques continue to improve, we anticipate further  
451 reductions in retrieval biases and increases in data coverage, leading to even more  
452 reliable, near real-time estimates of NH<sub>3</sub> fluxes.



#### 453 **4.2 Spatiotemporal pattern of NH<sub>3</sub> flux**

454 Beyond demonstrating robust satellite-based flux estimates, our analysis  
455 exposes clear spatial gradients and pronounced seasonality in NH<sub>3</sub> sources and sinks  
456 across the CONUS. Both IASI- and CrIS-derived fluxes identify consistent emission  
457 hotspots (Fig. 2) in the San Joaquin Valley (California), Snake River Valley (Idaho),  
458 Texas Panhandle, Great Plains, Southeastern Pennsylvania, and Eastern North  
459 Carolina (Fig. 4-9), characterized by intensive livestock operations and fertilizer  
460 application, which are consistent with existing maps of VCD hotspots (Chen et al.,  
461 2021; Wang et al., 2021) and emission mapping efforts (Evangelidou et al., 2021; Zhang  
462 et al., 2012; Sitwell et al., 2022). Other than emissions, our directional derivative  
463 approach can detect sinks in vegetation-dense areas surrounding these emission  
464 sources, such as shrublands and scrublands, forests, grasslands, and wetlands,  
465 highlighting the role of nearby ecosystems in capturing NH<sub>3</sub> through deposition (Pan  
466 et al., 2021; Hu et al., 2021; Azouz et al., 2019; Kharol et al., 2018; Loubet et al., 2009).  
467 This localized deposition has caused negative effects of excess nitrogen deposition in  
468 sensitive ecosystems (Krupa, 2003; Pearson and Stewart, 1993), and our results point  
469 to an upward trend in deposition (Fig. 11) that could amplify these impacts in the future.

470 Our results further indicate that deposition near sources is the predominant NH<sub>3</sub>  
471 removal pathway, rather than chemical transformation. This pattern is likely reflecting  
472 acid-limited conditions that suppress the formation of ammonium particulate matter  
473 (Pan et al., 2024). The relatively high dry deposition velocity of NH<sub>3</sub> (Hesterberg et al.,  
474 1996; Kirchner et al., 2005) and its slow chemical reaction rate with acidic species  
475 under acid-limited conditions (Sutton et al., 2009) reinforce the small contribution of  
476 chemical pathways to NH<sub>3</sub> removal in many agricultural hotspots. Consistent with  
477 recent modeling and observational studies (Luo et al., 2022; Warner et al., 2017), our  
478 multi-year analyses reveal a gradual but evident increase in NH<sub>3</sub> fluxes over time (Fig.  
479 11), raising concerns that expanding agricultural activities may be offsetting air quality  
480 gains achieved through reductions in nitrogen oxides (Li et al., 2016).

481 The seasonality of NH<sub>3</sub> fluxes (Fig. 11) is closely linked to meteorological factors  
482 and agricultural activities, with enhanced fluxes in warm months due to increased  
483 volatilization from livestock production and fertilizer application (Tang et al., 2018;  
484 Warner et al., 2017; Nelson et al., 2017) and relatively lower fluxes in winter. These  
485 seasonal signals underscore the importance of timely policy by controlling agricultural  
486 practices to manage NH<sub>3</sub> emissions and subsequent environmental impacts.  
487 Successful examples from Western Europe demonstrate that targeted regulations can  
488 effectively reduce NH<sub>3</sub> emissions (Liu et al., 2022). Furthermore, reducing ammonia  
489 emissions proves more cost-effective than controlling nitrogen oxides for mitigating  
490 PM<sub>2.5</sub> pollution (Gu et al., 2021). These findings emphasize the profound influence of  
491 agricultural practices and temperature regimes on NH<sub>3</sub> flux dynamics, underscoring  
492 the need for integrated strategies to address local and regional air quality concerns.



## 493 **5. Conclusion**

494 This study highlights the utility of the directional derivative approach applied to  
495 satellite data for estimating NH<sub>3</sub> fluxes across the CONUS. By leveraging IASI and  
496 CrIS observations, we addressed challenges related to spatial variability and seasonal  
497 signals, providing insights into NH<sub>3</sub> emission and deposition dynamics.

498 Our findings indicate that deposition serves as a significant removal pathway  
499 for NH<sub>3</sub>. NH<sub>3</sub> sinks were predominantly located near source regions, particularly in  
500 vegetation-dense areas where rapid deposition occurs. Major NH<sub>3</sub> emission hotspots  
501 were identified in agricultural regions, including the San Joaquin Valley in California,  
502 the Snake River Valley in Idaho, the Texas Panhandle, the Great Plains, Southeastern  
503 Pennsylvania, and Eastern North Carolina. NH<sub>3</sub> fluxes exhibited a clear seasonal  
504 pattern, peaking during warm months due to increased volatilization from agricultural  
505 activities and declining during winter. Increasing trends in NH<sub>3</sub> fluxes highlight the  
506 growing impact of intensified agricultural activities, emphasizing the need for improved  
507 monitoring and mitigation strategies. While satellite-derived NH<sub>3</sub> fluxes strongly  
508 aligned with bottom-up inventories, satellite observations offered additional value by  
509 capturing key hotspots and seasonal variabilities.

510 This study demonstrates the value of satellite observations for high-resolution  
511 monitoring of reactive nitrogen cycling, particularly in regions with limited ground-  
512 based measurements. These findings offer critical insights for understanding nitrogen  
513 loss and deposition processes, supporting enhanced nitrogen management strategies  
514 and environmental policy efforts aimed at mitigating ammonia's environmental impacts  
515 and managing reactive nitrogen in the atmosphere.

## 516 **Code and data availability**

517 The IASI L2 ammonia satellite observations are available from the AERIS data  
518 infrastructure (<https://doi.org/10.25326/10>, Clarisse et al., 2018). The CrIS L2  
519 ammonia satellite observations can be obtained by request to Mark Shephard  
520 ([mark.shephard@ec.gc.ca](mailto:mark.shephard@ec.gc.ca)). The ERA5 data are available at  
521 <https://doi.org/10.24381/cds.adbb2d47> (Hersbach et al., 2023). Code for flux  
522 estimation can be found at [https://github.com/Kang-Sun-CfA/Oversampling\\_matlab](https://github.com/Kang-Sun-CfA/Oversampling_matlab).

## 523 **Author contribution**

524 KS and KG designed the study and coordinated the paper. LC, MVD and PFC  
525 contributed to the IASI ammonia observations. KCP and MWS provided the CrIS  
526 ammonia observations. KS wrote the code for the directional derivative approach. ZL  
527 performed the estimations and analyses and wrote the paper. All the authors  
528 contributed to the final version of the paper.

## 529 **Competing interests**

530 The contact author has declared that neither of the authors has any competing  
531 interests.



532 **Acknowledgments**

533           The authors acknowledge support from NASA's Interdisciplinary Science (IDS)  
534 Program. KG and ZL acknowledge support from USDA NIFA and Hatch. KS  
535 acknowledges support from NSF CAREER (AGS 2338758).



## 536 References

- 537 Adams, C., McLinden, C. A., Shephard, M. W., Dickson, N., Dammers, E., Chen, J., Makar,  
538 P., Cady-Pereira, K. E., Tam, N., Kharol, S. K., Lamsal, L. N., and Krotkov, N. A.:  
539 Satellite-derived emissions of carbon monoxide, ammonia, and nitrogen dioxide from  
540 the 2016 Horse River wildfire in the Fort McMurray area, *Atmos. Chem. Phys.*, 19, 2577–  
541 2599, <https://doi.org/10.5194/acp-19-2577-2019>, 2019.
- 542 Asman, W. A. H., Sutton, M. A., and Schjørring, J. K.: Ammonia: emission, atmospheric  
543 transport and deposition, *New Phytologist*, 139, 27–48, <https://doi.org/10.1046/j.1469-8137.1998.00180.x>, 1998.
- 545 Ayazpour, Z., Sun, K., Zhang, R., and Shen, H.: Evaluation of the directional derivative  
546 approach for timely and accurate satellite-based emission estimation using chemical  
547 transport model simulation of nitrogen oxides, *ESS Open Archive*,  
548 <https://doi.org/10.22541/essoar.173046708.85066876/v1>, 2024.
- 549 Azouz, N., Drouet, J.-L., Beekmann, M., Siour, G., Wichink Kruit, R., and Cellier, P.:  
550 Comparison of spatial patterns of ammonia concentration and dry deposition flux  
551 between a regional Eulerian chemistry-transport model and a local Gaussian plume  
552 model, *Air Qual. Atmos. Health*, 12, 719–729, <https://doi.org/10.1007/s11869-019-00691-y>, 2019.
- 554 Behera, S. N. and Sharma, M.: Investigating the potential role of ammonia in ion chemistry of  
555 fine particulate matter formation for an urban environment, *Sci. Total Environ.*, 408,  
556 3569–3575, <https://doi.org/10.1016/j.scitotenv.2010.04.017>, 2010.
- 557 Beirle, S., Borger, C., Dörner, S., Li, A., Hu, Z., Liu, F., Wang, Y., and Wagner, T.: Pinpointing  
558 nitrogen oxide emissions from space, *Sci Adv*, 5, eaax9800,  
559 <https://doi.org/10.1126/sciadv.aax9800>, 2019.
- 560 Beirle, S., Borger, C., Dörner, S., Eskes, H., Kumar, V., de Laat, A., and Wagner, T.: Catalog  
561 of NO<sub>x</sub> emissions from point sources as derived from the divergence of the NO<sub>2</sub> flux for  
562 TROPOMI, *Earth Syst. Sci. Data*, 13, 2995–3012, <https://doi.org/10.5194/essd-13-2995-2021>, 2021.
- 564 Bouwman, A. F., Lee, D. S., Asman, W. A. H., Dentener, F. J., Van Der Hoek, K. W., and  
565 Olivier, J. G. J.: A global high-resolution emission inventory for ammonia, *Global  
566 Biogeochem. Cycles*, 11, 561–587, <https://doi.org/10.1029/97gb02266>, 1997.
- 567 van Breemen, N., Burrough, P. A., Velthorst, E. J., van Dobben, H. F., de Wit, T., Ridder, T.  
568 B., and Reijnders, H. F. R.: Soil acidification from atmospheric ammonium sulphate in  
569 forest canopy throughfall, *Nature*, 299, 548–550, <https://doi.org/10.1038/299548a0>,  
570 1982.
- 571 Byrne, B., Liu, J., Bowman, K. W., Pascolini-Campbell, M., Chatterjee, A., Pandey, S.,  
572 Miyazaki, K., van der Werf, G. R., Wunch, D., Wennberg, P. O., Roehl, C. M., and Sinha,  
573 S.: Carbon emissions from the 2023 Canadian wildfires, *Nature*, 633, 835–839,  
574 <https://doi.org/10.1038/s41586-024-07878-z>, 2024.
- 575 Cao, H., Henze, D. K., Shephard, M. W., Dammers, E., Cady-Pereira, K., Alvarado, M.,  
576 Lonsdale, C., Luo, G., Yu, F., Zhu, L., Danielson, C. G., and Edgerton, E. S.: Inverse  
577 modeling of NH<sub>3</sub> sources using CrIS remote sensing measurements, *Environ. Res. Lett.*,  
578 15, 104082, <https://doi.org/10.1088/1748-9326/abb5cc>, 2020.



- 579 Cao, H., Henze, D. K., Zhu, L., Shephard, M. W., Cady-Pereira, K., Dammers, E., Sitwell, M.,  
580 Heath, N., Lonsdale, C., Bash, J. O., Miyazaki, K., Flechard, C., Fauvel, Y., Kruit, R. W.,  
581 Feigenspan, S., Brümmer, C., Schrader, F., Twigg, M. M., Leeson, S., Tang, Y. S.,  
582 Stephens, A. C. M., Braban, C., Vincent, K., Meier, M., Seitler, E., Geels, C., Ellermann,  
583 T., Sanocka, A., and Capps, S. L.: 4D-Var inversion of European NH<sub>3</sub> emissions using  
584 CrIS NH<sub>3</sub> measurements and GEOS-chem adjoint with bi-directional and uni-directional  
585 flux schemes, *J. Geophys. Res.*, 127, e2021JD035687,  
586 <https://doi.org/10.1029/2021JD035687>, 2022.
- 587 Chang, Y., Zou, Z., Deng, C., Huang, K., Collett, J. L., Lin, J., and Zhuang, G.: The importance  
588 of vehicle emissions as a source of atmospheric ammonia in the megacity of Shanghai,  
589 *Atmos. Chem. Phys.*, 16, 3577–3594, <https://doi.org/10.5194/acp-16-3577-2016>, 2016.
- 590 Chen, Y., Shen, H., Kaiser, J., Hu, Y., Capps, S. L., Zhao, S., Hakami, A., Shih, J.-S., Pavur,  
591 G. K., Turner, M. D., Henze, D. K., Resler, J., Nenes, A., Napelenok, S. L., Bash, J. O.,  
592 Fahey, K. M., Carmichael, G. R., Chai, T., Clarisse, L., Coheur, P.-F., Van Damme, M.,  
593 and Russell, A. G.: High-resolution hybrid inversion of IASI ammonia columns to  
594 constrain US ammonia emissions using the CMAQ adjoint model, *Atmos. Chem. Phys.*,  
595 21, 2067–2082, <https://doi.org/10.5194/acp-21-2067-2021>, 2021.
- 596 Chen, Y., Shen, H., Kaiser, J., Hu, Y., Capps, S. L., Zhao, S., Hakami, A., Shih, J.-S., Pavur,  
597 G. K., Turner, M. D., Henze, D. K., Resler, J., Nenes, A., Napelenok, S. L., Bash, J. O.,  
598 Fahey, K. M., Carmichael, G. R., Chai, T., Clarisse, L., Coheur, P.-F., Van Damme, M.,  
599 and Russell, A. G.: High-resolution hybrid inversion of IASI ammonia columns to  
600 constrain US ammonia emissions using the CMAQ adjoint model, *Atmos. Chem. Phys.*,  
601 21, 2067–2082, <https://doi.org/10.5194/acp-21-2067-2021>, 2021.
- 602 Clarisse, L., Shephard, M. W., Dentener, F., Hurtmans, D., Cady-Pereira, K., Karagulian, F.,  
603 Van Damme, M., Clerbaux, C., and Coheur, P.-F.: Satellite monitoring of ammonia: A  
604 case study of the San Joaquin Valley, *Journal of Geophysical Research: Atmospheres*,  
605 115, <https://doi.org/10.1029/2009JD013291>, 2010.
- 606 Clarisse, L., Van Damme, M., and Coheur, P.-F.: Standard daily IASI/Metop-A ULB-LATMOS  
607 ammonia (NH<sub>3</sub>) L2 product (total column), <https://doi.org/10.25326/10>, 2018.
- 608 Clarisse, L., Franco, B., Van Damme, M., Di Gioacchino, T., Hadji-Lazaro, J., Whitburn, S.,  
609 Noppen, L., Hurtmans, D., Clerbaux, C., and Coheur, P.: The IASI NH<sub>3</sub> version 4  
610 product: averaging kernels and improved consistency, *Atmos. Meas. Tech.*, 16, 5009–  
611 5028, <https://doi.org/10.5194/amt-16-5009-2023>, 2023.
- 612 Clerbaux, C., Boynard, A., Clarisse, L., George, M., Hadji-Lazaro, J., Herbin, H., Hurtmans,  
613 D., Pommier, M., Razavi, A., Turquety, S., Wespes, C., and Coheur, P.: Monitoring of  
614 atmospheric composition using the thermal infrared IASI/METOP sounder, *Atmos.*  
615 *Chem. Phys.*, 9, 6041–6054, <https://doi.org/10.5194/ACP-9-6041-2009>, 2009.
- 616 Dammers, E., McLinden, C., Griffin, D., Shephard, M. W., Van Der Graaf, S., Lutsch, E.,  
617 Schaap, M., Gainairu-Matz, Y., Fioletov, V. E., Van Damme, M., Whitburn, S., Clarisse,  
618 L., Cady-Pereira, K. E., Clerbaux, C., Coheur, P. F., and Willem Erisman, J., NH<sub>3</sub>  
619 emissions from large point sources derived from CrIS and IASI satellite observations,  
620 *Atmos. Chem. Phys.*, 19, 12261–12293, <https://doi.org/10.5194/acp-19-12261-2019>,  
621 2019.
- 622 Dammers, E., Shephard, M. W., Palm, M., Cady-Pereira, K., Capps, S., Lutsch, E., Strong, K.,



- 623 Hannigan, J. W., Ortega, I., Toon, G. C., Stremme, W., Grutter, M., Jones, N., Smale,  
624 D., Siemons, J., Hrpcek, K., Tremblay, D., Schaap, M., Notholt, J., and Erisman, J. W.:  
625 Validation of the CrIS fast physical NH<sub>3</sub> retrieval with ground-based FTIR, *Atmos. Meas.*  
626 *Tech.*, 10, 2645–2667, <https://doi.org/10.5194/amt-10-2645-2017>, 2017.
- 627 Dentener, F. J. and Crutzen, P. J.: A three-dimensional model of the global ammonia cycle, *J.*  
628 *Atmos. Chem.*, 19, 331–369, <https://doi.org/10.1007/bf00694492>, 1994.
- 629 Erisman, J. W., Galloway, J. N., Seitzinger, S., Bleeker, A., Dise, N. B., Petrescu, A. M. R.,  
630 Leach, A. M., and de Vries, W.: Consequences of human modification of the global  
631 nitrogen cycle, *Philos. Trans. R. Soc. Lond. B Biol. Sci.*, 368, 20130116,  
632 <https://doi.org/10.1098/rstb.2013.0116>, 2013.
- 633 Evangeliou, N., Balkanski, Y., Eckhardt, S., Cozic, A., Van Damme, M., Coheur, P.-F.,  
634 Clarisse, L., Shephard, M. W., Cady-Pereira, K. E., and Hauglustaine, D.: 10-year  
635 satellite-constrained fluxes of ammonia improve performance of chemistry transport  
636 models, *Atmos. Chem. Phys.*, 21, 4431–4451, [https://doi.org/10.5194/acp-21-4431-](https://doi.org/10.5194/acp-21-4431-2021)  
637 [202110.5194/acp-21-4431-2021-supplement](https://doi.org/10.5194/acp-21-4431-2021-supplement), 2021.
- 638 Galloway, J. N., Aber, J. D., Erisman, J. W., Seitzinger, S. P., Howarth, R. W., Cowling, E. B.,  
639 and Cosby, B. J.: The nitrogen cascade, *Bioscience*, 53, 341,  
640 [https://doi.org/10.1641/0006-3568\(2003\)053\[0341:tnc\]2.0.co;2](https://doi.org/10.1641/0006-3568(2003)053[0341:tnc]2.0.co;2), 2003.
- 641 Galloway, J. N., Dentener, F. J., Capone, D. G., Boyer, E. W., Howarth, R. W., Seitzinger, S.  
642 P., Asner, G. P., Cleveland, C. C., Green, P. A., Holland, E. A., Karl, D. M., Michaels, A.  
643 F., Porter, J. H., Townsend, A. R., and Vöosmarty, C. J.: Nitrogen cycles: Past, present,  
644 and future, *Biogeochemistry*, 70, 153–226, <https://doi.org/10.1007/s10533-004-0370-0>,  
645 2004.
- 646 Gong, C., Tian, H., Liao, H., Pan, N., Pan, S., Ito, A., Jain, A. K., Kou-Giesbrecht, S., Joos, F.,  
647 Sun, Q., Shi, H., Vuichard, N., Zhu, Q., Peng, C., Maggi, F., Tang, F. H. M., and Zaehle,  
648 S.: Global net climate effects of anthropogenic reactive nitrogen, *Nature*, 632, 557–563,  
649 <https://doi.org/10.1038/s41586-024-07714-4>, 2024.
- 650 Gu, B., Zhang, L., Van Dingenen, R., Vieno, M., Van Grinsven, H. J., Zhang, X., Zhang, S.,  
651 Chen, Y., Wang, S., Ren, C., Rao, S., Holland, M., Winiwarter, W., Chen, D., Xu, J., and  
652 Sutton, M. A.: Abating ammonia is more cost-effective than nitrogen oxides for mitigating  
653 PM<sub>2.5</sub> air pollution, *Science*, 374, 758–762, <https://doi.org/10.1126/science.abf8623>,  
654 2021.
- 655 Heil, G. W. and Diemont, W. H.: Raised nutrient levels change heathland into grassland,  
656 *Vegetatio*, 53, 113–120, <https://doi.org/10.1007/bf00043031>, 1983.
- 657 Hersbach, H., Bell, B., Berrisford, P., Hirahara, S., Horányi, A., Muñoz-Sabater, J., Nicolas, J.,  
658 Peubey, C., Radu, R., Schepers, D., Simmons, A., Soci, C., Abdalla, S., Abellan, X.,  
659 Balsamo, G., Bechtold, P., Biavati, G., Bidlot, J., Bonavita, M., De Chiara, G., Dahlgren,  
660 P., Dee, D., Diamantakis, M., Dragani, R., Flemming, J., Forbes, R., Fuentes, M., Geer,  
661 A., Haimberger, L., Healy, S., Hogan, R. J., Hólm, E., Janisková, M., Keeley, S.,  
662 Laloyaux, P., Lopez, P., Lupu, C., Radnoti, G., de Rosnay, P., Rozum, I., Vamborg, F.,  
663 Villaume, S., and Jean-Noël Thépaut: The ERA5 global reanalysis, *Quart. J. Roy.*  
664 *Meteor. Soc.*, 146, 1999–2049, <https://doi.org/10.1002/qj.3803>, 2020.
- 665 Hersbach, H., Bell, B., Berrisford, P., Biavati, G., Horányi, A., Muñoz-Sabater, J., Nicolas, J.,



- 666 Peubey, C., Radu, R., Rozum, I., Schepers, D., Simmons, A., Soci, C., Dee, D., and  
667 Thépaut, J.-N.: ERA5 hourly data on single levels from 1940 to present,  
668 <https://doi.org/10.24381/CDS.ADBB2D47>, 2023.
- 669 Hesterberg, R., Blatter, A., Fahrni, M., Rosset, M., Neftel, A., Eugster, W., and Wanner, H.:  
670 Deposition of nitrogen-containing compounds to an extensively managed grassland in  
671 central Switzerland, *Environ. Pollut.*, 91, 21–34, [https://doi.org/10.1016/0269-7491\(95\)00036-q](https://doi.org/10.1016/0269-7491(95)00036-q), 1996.
- 673 Hu, C., Griffis, T. J., Frie, A., Baker, J. M., Wood, J. D., Millet, D. B., Yu, Z., Yu, X., and  
674 Czarnetzki, A. C.: A multiyear constraint on ammonia emissions and deposition within  
675 the US corn belt, *Geophys. Res. Lett.*, 48, e2020GL090865,  
676 <https://doi.org/10.1029/2020gl090865>, 2021.
- 677 Kharol, S. K., Shephard, M. W., McLinden, C. A., Zhang, L., Sioris, C. E., O'Brien, J. M., Vet,  
678 R., Cady-Pereira, K. E., Hare, E., Siemons, J., and Krotkov, N. A.: Dry deposition of  
679 reactive nitrogen from satellite observations of ammonia and nitrogen dioxide over north  
680 America, *Geophys. Res. Lett.*, 45, 1157–1166, <https://doi.org/10.1002/2017gl075832>,  
681 2018.
- 682 Kirchner, M., Jakobi, G., Feicht, E., Bernhardt, M., and Fischer, A.: Elevated NH<sub>3</sub> and NO<sub>2</sub> air  
683 concentrations and nitrogen deposition rates in the vicinity of a highway in Southern  
684 Bavaria, *Atmos. Environ.* (1994), 39, 4531–4542,  
685 <https://doi.org/10.1016/j.atmosenv.2005.03.052>, 2005.
- 686 Krupa, S. V.: Effects of atmospheric ammonia (NH<sub>3</sub>) on terrestrial vegetation: a review,  
687 *Environ. Pollut.*, 124, 179–221, [https://doi.org/10.1016/s0269-7491\(02\)00434-7](https://doi.org/10.1016/s0269-7491(02)00434-7), 2003.
- 688 Lin, H., Jacob, D. J., Lundgren, E. W., Sulprizio, M. P., Keller, C. A., Fritz, T. M., Eastham, S.  
689 D., Emmons, L. K., Campbell, P. C., Baker, B., Saylor, R. D., and Montuoro, R.:  
690 Harmonized Emissions Component (HEMCO) 3.0 as a versatile emissions component  
691 for atmospheric models: application in the GEOS-Chem, NASA GEOS, WRF-GC,  
692 CESM2, NOAA GEFS-Aerosol, and NOAA UFS models, *Geosci. Model Dev.*, 14, 5487–  
693 5506, <https://doi.org/10.5194/gmd-14-5487-2021>, 2021.
- 694 Liu, L., Zhang, X., Wong, A. Y. H., Xu, W., Liu, X., Li, Y., Mi, H., Lu, X., Zhao, L., Wang, Z.,  
695 Wu, X., and Wei, J.: Estimating global surface ammonia concentrations inferred from  
696 satellite retrievals, *Atmos. Chem. Phys.*, 19, 12051–12066, <https://doi.org/10.5194/acp-19-12051-2019>, 2019.
- 698 Liu, L., Xu, W., Lu, X., Zhong, B., Guo, Y., Lu, X., Zhao, Y., He, W., Wang, S., Zhang, X., Liu,  
699 X., and Vitousek, P.: Exploring global changes in agricultural ammonia emissions and  
700 their contribution to nitrogen deposition since 1980, *Proc. Natl. Acad. Sci. U. S. A.*, 119,  
701 e2121998119, <https://doi.org/10.1073/pnas.2121998119>, 2022.
- 702 Li, Y., Schichtel, B. A., Walker, J. T., Schwede, D. B., Chen, X., Lehmann, C. M. B., Puchalski,  
703 M. A., Gay, D. A., and Collett, J. L., Jr: Increasing importance of deposition of reduced  
704 nitrogen in the United States, *Proc. Natl. Acad. Sci. U. S. A.*, 113, 5874–5879,  
705 <https://doi.org/10.1073/pnas.1525736113>, 2016.
- 706 Lonsdale, C. R. and Sun, K.: Nitrogen oxides emissions from selected cities in North America,  
707 Europe, and East Asia observed by the TROPOspheric Monitoring Instrument  
708 (TROPOMI) before and after the COVID-19 pandemic, *Atmos. Chem. Phys.*, 23, 8727–



- 709 8748, <https://doi.org/10.5194/acp-23-8727-2023>, 2023.
- 710 Loubet, B., Asman, W. A. H., Theobald, M. R., Hertel, O., Tang, Y. S., Robin, P., Hassouna,  
711 M., Dämmgen, U., Genermont, S., Cellier, P., and Sutton, M. A.: Ammonia deposition  
712 near hot spots: Processes, models and monitoring methods, in: *Atmospheric Ammonia*,  
713 Springer Netherlands, Dordrecht, 205–267, [https://doi.org/10.1007/978-1-4020-9121-](https://doi.org/10.1007/978-1-4020-9121-6_15)  
714 [6\\_15](https://doi.org/10.1007/978-1-4020-9121-6_15), 2009.
- 715 Luo, Z., Zhang, Y., Chen, W., Van Damme, M., Coheur, P.-F., and Clarisse, L.: Estimating  
716 global ammonia (NH<sub>3</sub>) emissions based on IASI observations from 2008 to 2018, *Atmos.*  
717 *Chem. Phys.*, 22, 10375–10388, <https://doi.org/10.5194/acp-22-10375-2022>, 2022.
- 718 Ma, R., Li, K., Guo, Y., Zhang, B., Zhao, X., Linder, S., Guan, C., Chen, G., Gan, Y., and Meng,  
719 J.: Mitigation potential of global ammonia emissions and related health impacts in the  
720 trade network, *Nat. Commun.*, 12, 6308, <https://doi.org/10.1038/s41467-021-25854-3>,  
721 2021.
- 722 Marais, E. A., Pandey, A. K., Van Damme, M., Clarisse, L., Coheur, P.-F., Shephard, M. W.,  
723 Cady-Pereira, K. E., Misselbrook, T., Zhu, L., Luo, G., and Yu, F.: UK ammonia  
724 emissions estimated with satellite observations and GEOS-chem, *J. Geophys. Res.*,  
725 126, <https://doi.org/10.1029/2021jd035237>, 2021.
- 726 Nelson, A. J., Koloutsou-Vakakis, S., Rood, M. J., Myles, L., Lehmann, C., Bernacchi, C.,  
727 Balasubramanian, S., Joo, E., Heuer, M., Vieira-Filho, M., and Lin, J.: Season-long  
728 ammonia flux measurements above fertilized corn in central Illinois, USA, using relaxed  
729 eddy accumulation, *Agric. For. Meteorol.*, 239, 202–212,  
730 <https://doi.org/10.1016/j.agrformet.2017.03.010>, 2017.
- 731 Pan, D., Benedict, K. B., Golston, L. M., Wang, R., Collett, J. L., Jr, Tao, L., Sun, K., Guo, X.,  
732 Ham, J., Prenni, A. J., Schichtel, B. A., Mikoviny, T., Müller, M., Wisthaler, A., and  
733 Zondlo, M. A.: Ammonia dry deposition in an alpine ecosystem traced to agricultural  
734 emission hotspots, *Environ. Sci. Technol.*, 55, 7776–7785,  
735 <https://doi.org/10.1021/acs.est.0c05749>, 2021.
- 736 Pan, D., Mauzerall, D. L., Wang, R., Guo, X., Puchalski, M., Guo, Y., Song, S., Tong, D.,  
737 Sullivan, A. P., Schichtel, B. A., Collett, J. L., Jr, and Zondlo, M. A.: Regime shift in  
738 secondary inorganic aerosol formation and nitrogen deposition in the rural United States,  
739 *Nat. Geosci.*, 17, 617–623, <https://doi.org/10.1038/s41561-024-01455-9>, 2024.
- 740 Pearson, J. and Stewart, G. R.: The deposition of atmospheric ammonia and its effects on  
741 plants, *New Phytol.*, 125, 283–305, <https://doi.org/10.1111/j.1469-8137.1993.tb03882.x>,  
742 1993.
- 743 Reche, C., Viana, M., Karanasiou, A., Cusack, M., Alastuey, A., Artiñano, B., Revuelta, M. A.,  
744 López-Mahía, P., Blanco-Heras, G., Rodríguez, S., Sánchez de la Campa, A. M.,  
745 Fernández-Camacho, R., González-Castanedo, Y., Mantilla, E., Tang, Y. S., and  
746 Querol, X.: Urban NH<sub>3</sub> levels and sources in six major Spanish cities, *Chemosphere*,  
747 119, 769–777, <https://doi.org/10.1016/j.chemosphere.2014.07.097>, 2015.
- 748 Shephard, M. W. and Cady-Pereira, K.E.: Cross-track Infrared Sounder (CrIS) Satellite  
749 Observations of Tropospheric Ammonia, *Atmos. Meas. Tech.*, 8, 1323–1336,  
750 <https://doi.org/10.5194/amt-8-1323-2015>, 2015.
- 751 Shephard, M. W., Dammers, E., Cady-Pereira, K. E., Kharol, S. K., Thompson, J., Gainariu-



- 752 Matz, Y., Zhang, J., McLinden, C. A., Kovachik, A., Moran, M., Bittman, S., Sioris, C. E.,  
753 Griffin, D., Alvarado, M. J., Lonsdale, C., Savic-Jovicic, V., and Zheng, Q.: Ammonia  
754 measurements from space with the Cross-track Infrared Sounder: characteristics and  
755 applications, *Atmos. Chem. Phys.*, 20, 2277–2302, [https://doi.org/10.5194/acp-20-2277-](https://doi.org/10.5194/acp-20-2277-2020)  
756 2020, 2020.
- 757 Sitwell, M., Shephard, M. W., Rochon, Y., Cady-Pereira, K., and Dammers, E.: An ensemble-  
758 variational inversion system for the estimation of ammonia emissions using CrIS satellite  
759 ammonia retrievals, *Atmos. Chem. Phys.*, 22, 6595–6624, [https://doi.org/10.5194/acp-](https://doi.org/10.5194/acp-22-6595-2022)  
760 22-6595-2022, 2022.
- 761 Sun, K.: Derivation of emissions from satellite-observed column amounts and its application  
762 to TROPOMI NO<sub>2</sub> and CO observations, *Geophys. Res. Lett.*, 49,  
763 <https://doi.org/10.1029/2022gl101102>, 2022.
- 764 Sun, K., Tao, L., Miller, D. J., Pan, D., Golston, L. M., Zondlo, M. A., Griffin, R. J., Wallace, H.  
765 W., Leong, Y. J., Yang, M. M., Zhang, Y., Mauzerall, D. L., and Zhu, T.: Vehicle  
766 emissions as an important urban ammonia source in the United States and China,  
767 *Environ. Sci. Technol.*, 51, 2472–2481, <https://doi.org/10.1021/acs.est.6b02805>, 2017.
- 768 Sun, K., Zhu, L., Cady-Pereira, K., Chan Miller, C., Chance, K., Clarisse, L., Coheur, P.-F.,  
769 González Abad, G., Huang, G., Liu, X., Van Damme, M., Yang, K., and Zondlo, M.: A  
770 physics-based approach to oversample multi-satellite, multispecies observations to a  
771 common grid, *Atmos. Meas. Tech.*, 11, 6679–6701, [https://doi.org/10.5194/amt-11-](https://doi.org/10.5194/amt-11-6679-2018)  
772 6679-2018, 2018.
- 773 Sutton, M., Reis, S., and Baker, S. (Eds.): *Atmospheric Ammonia: Detecting emission changes  
774 and environmental impacts. Results of an Expert Workshop under the Convention on  
775 Long-range Transboundary Air Pollution*, 1st ed., Springer, New York, NY, 464 pp.,  
776 <https://doi.org/10.1007/978-1-4020-9121-6>, 2009.
- 777 Sutton, M. A., Erisman, J. W., Dentener, F., and Möller, D.: Ammonia in the environment: from  
778 ancient times to the present, *Environ. Pollut.*, 156, 583–604,  
779 <https://doi.org/10.1016/j.envpol.2008.03.013>, 2008.
- 780 Sutton, M. A., Reis, S., Riddick, S. N., Dragosits, U., Nemitz, E., Theobald, M. R., Tang, Y. S.,  
781 Braban, C. F., Vieno, M., Dore, A. J., Mitchell, R. F., Wanless, S., Daunt, F., Fowler, D.,  
782 Blackall, T. D., Milford, C., Flechard, C. R., Loubet, B., Massad, R., Cellier, P., Personne,  
783 E., Coheur, P. F., Clarisse, L., Van Damme, M., Ngadi, Y., Clerbaux, C., Skjæth, C. A.,  
784 Geels, C., Hertel, O., Wichink Kruit, R. J., Pinder, R. W., Bash, J. O., Walker, J. T.,  
785 Simpson, D., Horváth, L., Misselbrook, T. H., Bleeker, A., Dentener, F., and de Vries,  
786 W.: Towards a climate-dependent paradigm of ammonia emission and deposition,  
787 *Philos. Trans. R. Soc. Lond. B Biol. Sci.*, 368, 20130166,  
788 <https://doi.org/10.1098/rstb.2013.0166>, 2013.
- 789 Sutton, M. A., van Dijk, N., Levy, P. E., Jones, M. R., Leith, I. D., Sheppard, L. J., Leeson, S.,  
790 Sim Tang, Y., Stephens, A., Braban, C. F., Dragosits, U., Howard, C. M., Vieno, M.,  
791 Fowler, D., Corbett, P., Naikoo, M. I., Munzi, S., Ellis, C. J., Chatterjee, S., Steadman,  
792 C. E., Möring, A., and Wolseley, P. A.: Alkaline air: changing perspectives on nitrogen  
793 and air pollution in an ammonia-rich world, *Philos. Trans. A Math. Phys. Eng. Sci.*, 378,  
794 20190315, <https://doi.org/10.1098/rsta.2019.0315>, 2020.
- 795 Tang, Y. S., Braban, C. F., Dragosits, U., Dore, A. J., Simmons, I., van Dijk, N., Poskitt, J., Dos



- 796 Santos Pereira, G., Keenan, P. O., Conolly, C., Vincent, K., Smith, R. I., Heal, M. R., and  
797 Sutton, M. A.: Drivers for spatial, temporal and long-term trends in atmospheric ammonia  
798 and ammonium in the UK, *Atmos. Chem. Phys.*, 18, 705–733,  
799 <https://doi.org/10.5194/acp-18-705-2018>, 2018.
- 800 Tian, H., Xu, R., Canadell, J. G., Thompson, R. L., Winiwarter, W., Suntharalingam, P.,  
801 Davidson, E. A., Ciais, P., Jackson, R. B., Janssens-Maenhout, G., Prather, M. J.,  
802 Regnier, P., Pan, N., Pan, S., Peters, G. P., Shi, H., Tubiello, F. N., Zaehle, S., Zhou, F.,  
803 Arneth, A., Battaglia, G., Berthet, S., Bopp, L., Bouwman, A. F., Buitenhuis, E. T., Chang,  
804 J., Chipperfield, M. P., Dangal, S. R. S., Dlugokencky, E., Elkins, J. W., Eyre, B. D., Fu,  
805 B., Hall, B., Ito, A., Joos, F., Krummel, P. B., Landolfi, A., Laruelle, G. G., Lauerwald, R.,  
806 Li, W., Lienert, S., Maavara, T., MacLeod, M., Millet, D. B., Olin, S., Patra, P. K., Prinn,  
807 R. G., Raymond, P. A., Ruiz, D. J., van der Werf, G. R., Vuichard, N., Wang, J., Weiss,  
808 R. F., Wells, K. C., Wilson, C., Yang, J., and Yao, Y.: A comprehensive quantification of  
809 global nitrous oxide sources and sinks, *Nature*, 586, 248–256,  
810 <https://doi.org/10.1038/s41586-020-2780-0>, 2020.
- 811 Van Damme, M., Clarisse, L., Whitburn, S., Hadji-Lazaro, J., Hurtmans, D., Clerbaux, C., and  
812 Coheur, P.-F.: Industrial and agricultural ammonia point sources exposed, *Nature*, 564,  
813 99–103, <https://doi.org/10.1038/s41586-018-0747-1>, 2018.
- 814 Vira, J., Hess, P., Ossouhou, M., and Galy-Lacaux, C.: Evaluation of interactive and prescribed  
815 agricultural ammonia emissions for simulating atmospheric composition in CAM-chem,  
816 *Atmos. Chem. Phys.*, 22, 1883–1904, <https://doi.org/10.5194/acp-22-1883-2022>, 2022.
- 817 Wang, R., Guo, X., Pan, D., Kelly, J. T., Bash, J. O., Sun, K., Paulot, F., Clarisse, L., Van  
818 Damme, M., Whitburn, S., Coheur, P.-F., Clerbaux, C., and Zondlo, M. A.: Monthly  
819 patterns of ammonia over the contiguous United States at 2-km resolution, *Geophys.  
820 Res. Lett.*, 48, <https://doi.org/10.1029/2020gl090579>, 2021.
- 821 Wang, R., Pan, D., Guo, X., Sun, K., Clarisse, L., Van Damme, M., Coheur, P.-F., Clerbaux,  
822 C., Puchalski, M., and Zondlo, M. A.: Bridging the spatial gaps of the Ammonia  
823 Monitoring Network using satellite ammonia measurements, *Atmos. Chem. Phys.*, 23,  
824 13217–13234, <https://doi.org/10.5194/acp-23-13217-2023>, 2023.
- 825 Wang, S., Nan, J., Shi, C., Fu, Q., Gao, S., Wang, D., Cui, H., Saiz-Lopez, A., and Zhou, B.:  
826 Atmospheric ammonia and its impacts on regional air quality over the megacity of  
827 Shanghai, China, *Sci. Rep.*, 5, 15842, <https://doi.org/10.1038/srep15842>, 2015.
- 828 Warner, J. X., Dickerson, R. R., Wei, Z., Strow, L. L., Wang, Y., and Liang, Q.: Increased  
829 atmospheric ammonia over the world's major agricultural areas detected from space:  
830 Global Atmospheric NH<sub>3</sub> Year Trends, *Geophys. Res. Lett.*, 44, 2875–2884,  
831 <https://doi.org/10.1002/2016GL072305>, 2017.
- 832 Zhang, L., Jacob, D. J., Knipping, E. M., Kumar, N., Munger, J. W., Carouge, C. C., van  
833 Donkelaar, A., Wang, Y. X., and Chen, D.: Nitrogen deposition to the United States:  
834 distribution, sources, and processes, *Atmos. Chem. Phys.*, 12, 4539–4554,  
835 <https://doi.org/10.5194/acp-12-4539-2012>, 2012.
- 836 Zhang, L., Chen, Y., Zhao, Y., Henze, D. K., Zhu, L., Song, Y., Paulot, F., Liu, X., Pan, Y., Lin,  
837 Y., and Huang, B.: Agricultural ammonia emissions in China: reconciling bottom-up and  
838 top-down estimates, *Atmos. Chem. Phys.*, 18, 339–355, <https://doi.org/10.5194/acp-18-339-2018>, 2018.



840 Zhu, L., Henze, D. K., Cady-Pereira, K. E., Shephard, M. W., Luo, M., Pinder, R. W., Bash, J.  
841 O., and Jeong, G.-R.: Constraining U.S. ammonia emissions using TES remote sensing  
842 observations and the GEOS-Chem adjoint model: INVERSE MODELING OF  
843 NH<sub>3</sub>EMISSIONS, *J. Geophys. Res.*, 118, 3355–3368,  
844 <https://doi.org/10.1002/jgrd.50166>, 2013.